Mandal *et al. Biochar* (2026) 8:9
https://doi.org/10.1007/s42773-025-00510-x

Biochar

ORIGINAL RESEARCH

Open Access

Temperature-modulated surface features of neem seed biochar for sustainable thermal energy storage applications

Soumen Mandal[1], Avinash C. Mendhe[2], Taejoon Park[3*] and Han Seung Lee[4*]

Abstract

Addressing the surging global energy demand while mitigating environmental degradation necessitates a paradigm shift from conventional energy systems to sustainable alternatives. However, the inherent intermittency of renewable energy sources mandates efficient harvesting mechanisms and advanced storage technologies to ensure uninterrupted energy availability. Thus, optimizing energy generation and storage systems is imperative for maximizing renewable energy utilization and advancing carbon neutrality. Biochar-based phase change materials (PCMs) emerge as a viable solution, simultaneously enhancing thermal energy storage efficiency and contributing to carbon sequestration. This study synthesizes biochar-based PCM composites using Neem (Azadirachta indica) seed-derived biochar, produced at two distinct pyrolysis temperatures (300 °C and 500 °C), and impregnated with lauric acid (LA). Comprehensive characterization through BET surface area analysis, FT-IR spectroscopy, SEM–EDS, DSC, and TGA evaluated the structural, chemical, and thermal properties of the composites. The biochar pyrolyzed at 500 °C exhibits a significantly higher surface area (668 m^2/g), facilitating enhanced PCM loading. FT-IR analysis confirmed the successful impregnation of LA while preserving its molecular structure, while SEM analysis revealed a highly porous biochar network that optimizes PCM accommodation. DSC and TGA results demonstrated an impressive latent heat storage capacity up to 94.92 J/g, stable phase transition behavior, and improved thermal stability. Leakage tests and infrared thermal imaging further validated the composites' shape-stabilizing efficiency, ensuring controlled heat absorption and dissipation without PCM leakage. By utilizing waste biomass, this study presents a sustainable and cost-effective approach to advanced thermal management, contributing to enhanced energy conservation and a reduced carbon footprint.

Keywords Biochar, Thermal energy storage, Porosity, Enthalpy, Heat flow

---

*Correspondence:
Taejoon Park
taejoon@hanyang.ac.kr
Han Seung Lee
ercleehs@hanyang.ac.kr
Full list of author information is available at the end of the article

Graphical Abstract

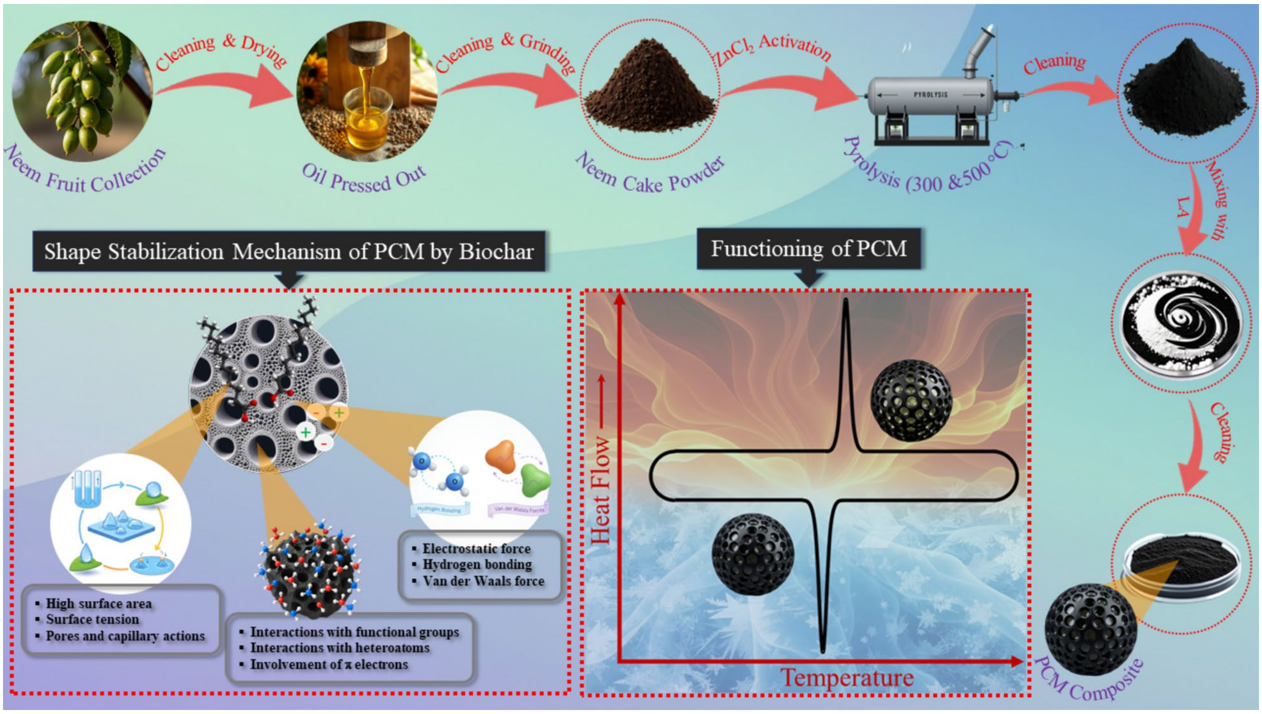

1 Introduction

In the quest to achieve carbon neutrality, optimizing energy generation and storage systems is of paramount importance. Carbon neutrality refers to a state where the amount of carbon dioxide emitted into the atmosphere is balanced by an equivalent amount of carbon removed or sequestered, thus resulting in net-zero emissions (Chen et al. 2022; Koh et al. 2023). This balance is crucial in the fight against climate change, as reducing the concentration of greenhouse gases is essential for stabilizing global temperatures and preventing environmental degradation (Wang et al. 2024). However, attaining carbon neutrality is not straightforward and requires innovative, forward-thinking strategies that can simultaneously reduce carbon emissions and provide a reliable, sustainable energy supply. The transition from traditional fossil fuels to renewable energy sources, such as solar, wind, and hydropower, is an important step toward this goal (Chien et al. 2022; Hao et al. 2023; Islam et al. 2024). Yet, the intermittent nature of these renewable sources presents a challenge, as energy supply can fluctuate based on environmental factors (Farghali et al. 2023; Nirbheram et al. 2024). This is where the optimization of energy storage systems becomes critical. Efficient energy storage not only ensures a stable supply by storing excess energy for use during periods of low generation but also enhances the overall sustainability of energy systems (Jafarian et al. 2024; Serat 2024). Developing advanced energy storage technologies and integrating sustainable materials are essential steps toward reaching carbon neutrality while maintaining energy security (Ishak et al. 2021a; Wang et al. 2021). Traditional energy storage systems, such as lithium-ion batteries, have limitations including high costs, finite material resources, and environmental concerns associated with mining (Gutsch and Leker 2024; Yang et al. 2021). Moreover, the energy loss during storage and retrieval processes can further reduce the overall efficiency of these systems (Lin et al. 2023). As a result, there is an urgent need for more sustainable, efficient, and cost-effective energy storage solutions.

One promising avenue is the integration of biochar-based phase change materials (PCMs) in energy storage systems, which can help to reduce carbon footprints while enhancing the efficiency and sustainability of energy usage (Ishak et al. 2023, 2024; Katish et al. 2024). PCMs offer a highly efficient method of thermal energy storage (TES). PCMs work by absorbing and releasing thermal energy during phase transitions, typically from solid to liquid and back again (Ishak et al. 2020, 2021a). During these transitions, PCMs can store large amounts of heat (Ishak et al. 2021b), making them ideal for use in applications where thermal regulation is important, such as in building heating and cooling systems (Jiang et al. 2024; Tyagi et al. 2021), solar power plants (Ismail et al. 2024; Wang et al. 2019), and industrial processes (Martínez et al. 2025; Yan and Mu 2025). However, conventional PCMs have limitations. Many common PCMs, such as paraffin and fatty acids, suffer from issues like low thermal conductivity, leakage during the melting process, and poor shape stability over multiple heating and cooling cycles (Mandal 2024; Mandal et al. 2022c). These issues have motivated researchers to explore ways to enhance the performance of PCMs.

Biochar, a carbon-rich material produced from the pyrolysis of organic biomass under low/restricted oxygen conditions (Ehsani and Parsimehr 2020), presents a sustainable and versatile additive to improve the properties of PCMs (Kumar and Kumar 2024; Soni and Panwar 2024). Biochar is particularly attractive due to its environmental benefits, as it sequesters carbon and can be sourced from waste biomass materials, making it a carbon-negative material (Parsimehr and Ehsani 2020b, a; Parsimehr et al. 2021; Senadheera et al. 2024; Zou et al. 2024a). Incorporating biochar into PCMs provides several advantages. First, biochar improves the heat transfer efficacy of the PCM, facilitating faster and more effective thermal management (Liang et al. 2023). This improvement is crucial for applications where rapid thermal cycling is required, such as in solar energy storage systems (Kumar and Kumar 2024). Additionally, biochar helps to stabilize the shape of the PCM, reducing the risk of material leakage during the phase transition process (Soni and Panwar 2024). This stability not only improves the reliability of the energy storage system but also extends its lifespan. Furthermore, biochar's porous structure increases the surface area available for thermal interaction, improving the overall energy storage capacity (Mandal et al. 2023a, 2022a). By optimizing the composition and processing conditions of biochar-based PCMs, it is possible to achieve a more effective and durable energy storage system.

To fully realize the potential of biochar-based PCMs, ongoing research focuses on optimizing their performance across several dimensions (Liang et al. 2023; Zhang et al. 2024a, 2024b). The temperature at which biochar is produced significantly affects its properties (Atinafu et al. 2025). Higher pyrolysis temperatures tend to increase biochar's surface area and porosity, which can enhance the thermal performance of PCMs. However, trade-offs must be considered, as extremely high temperatures may reduce biochar's structural integrity (Muhammad et al. 2022; Rambhatla et al. 2025). Additionally, the compatibility between biochar and the base PCM material is crucial. Ensuring that the PCM is well-integrated within the porous biochar matrix is necessary to maximize heat transfer and minimize agglomeration. Surface modifications to biochar, such as chemical treatments, can further improve its interaction with the PCM, enhancing thermal properties and shape stabilization.

The integration of biochar-based PCMs into energy storage systems offers a dual benefit for carbon neutrality. First, biochar itself serves as a carbon sink, sequestering carbon that would otherwise contribute to atmospheric CO_2 levels. Second, the improved performance of energy storage systems enabled by biochar-based PCMs enhances the efficiency of renewable energy systems, reducing the overall need for fossil fuels and lowering greenhouse gas emissions (Mandal et al. 2023b). By optimizing energy generation through renewable sources and integrating biochar shape stabilized PCMs into energy storage, the overall carbon footprint of energy systems can be significantly reduced (Jia et al. 2024; Kouchachvili et al. 2024). These technologies can play a pivotal role in achieving a sustainable energy future that aligns with the goals of carbon neutrality.

Through continued research and optimization of these materials, biochar-based PCMs can contribute significantly to the development of efficient, sustainable, and environmentally friendly energy systems. These advancements will help drive the transition toward a carbon–neutral world, addressing both energy challenges and climate change mitigation. Therefore, this study aims to understand the effect of the pyrolysis temperature for synthesizing biochar and its effect on the shape stabilization of PCMs. Neem (Azadirachta indica) seeds were chosen as biomass to synthesize porous biochars at two different temperatures. Neem seeds, an abundantly available agricultural by-product, are selected as the carbon precursor due to their high lignocellulosic content and widespread availability in tropical regions. Often discarded after oil extraction, neem seeds pose environmental concerns if unmanaged. Converting them into biochar not only promotes sustainable waste utilization but also yields a porous, carbon-rich material suitable for energy storage applications. Preliminary trials at higher pyrolysis temperatures (750 °C and 1000 °C) resulted in reduced surface area, minimal functional groups, and poor mechanical integrity. Thus, the study focused on biochars prepared at 300 °C and 500 °C, which demonstrated superior performance and stability. Lauric acid as PCM was integrated into the biochar pores for synthesizing the shape stable PCM. Different characterization techniques were employed to examine the biochars and shape stable PCMs. The novelty of this study lies in the utilization of neem seed, an underexploited biomass waste, for synthesizing porous biochar suitable for shape-stabilized PCM

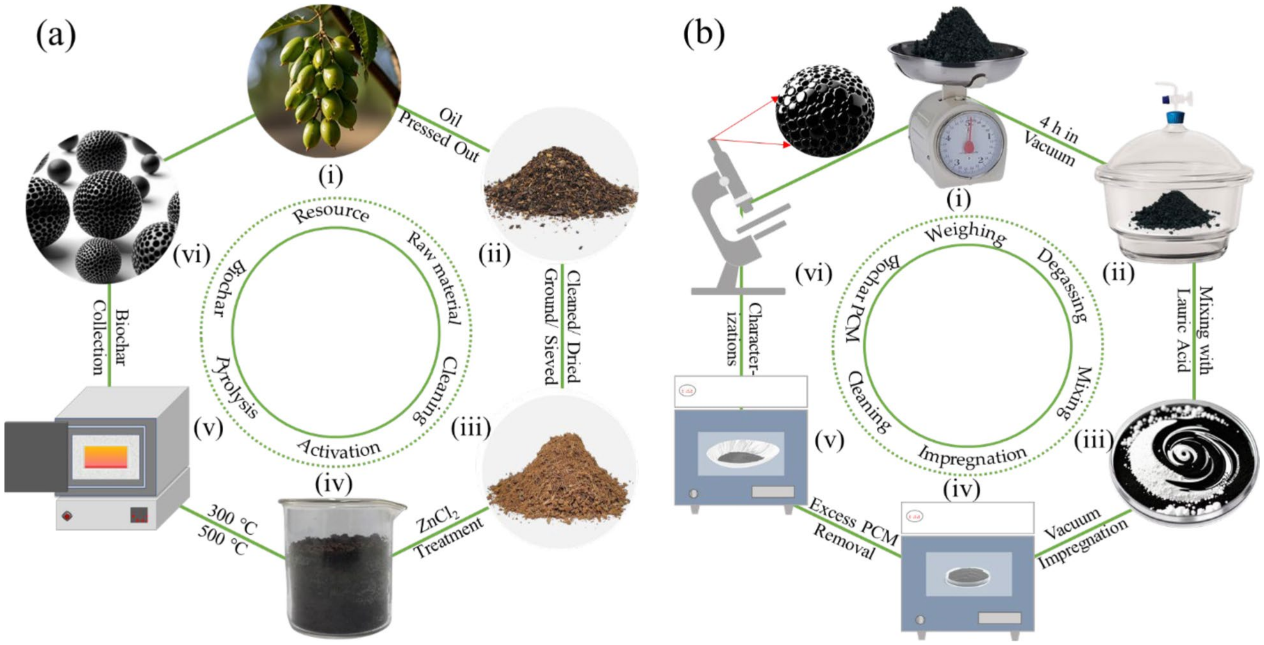

Fig. 1 Schematics of (**a**) biochar synthesis, and (**b**) shape stabilization process of LA. Roman numerals indicate sequential steps, marking the starting point and progression of each process

composites. This approach not only offers a sustainable route for biomass valorization but also contributes to the development of eco-friendly materials for thermal energy storage applications. The efforts made in this study intend to contribute to a more reliable and sustainable energy infrastructure, driving the global transition towards carbon neutrality.

2 Materials and methods

2.1 Materials

The Lauric acid (LA) was purchased from DUKSAN reagents, South Korea and was used without any further purification. The biochar used in this study was synthesized from the seeds of Neem (Azadirachta indica). Neem cake powder is made of Neem seeds after pressing out the oil inside the seeds. Neem cake powder was procured from the Indian market and cleaned with distilled water to remove dirt and impurities. Subsequently, the Neem cake powder was dried at 100 ℃ for 12 h. Then, the powder was ground using a grinder and sieved using mesh (50 mesh).

The resulting powder was activated in a 2 M $ZnCl_2$ aqueous solution at a ratio of 1 kg powder to 1 L solution and kept overnight at ambient conditions. After activation, the powder was placed in an alumina crucible with a fitted lid and transferred into an electrical muffle furnace. The furnace chamber was initially flushed with nitrogen gas to displace atmospheric oxygen and then partially filled with nitrogen to maintain an inert atmosphere during thermal treatment. Pyrolysis was carried out at two different temperatures, 300℃ and 500 ℃. Following pyrolysis, the samples were removed from the furnace and rigorously washed with distilled water to remove residual $ZnCl_2$. Finally, the biochar samples were dried in an oven at 100 ℃ for 12 h. The neem cake powder pyrolyzed at 300 ℃ and 500 ℃ were designated as NB-300 and NB-500, respectively. The synthesis scheme of the biochar is illustrated in Fig. 1a.

2.2 Shape stabilization method of LA

The LA was impregnated into the biochars by vacuum impregnation method. At the initial stage, the biochars were put inside the vacuum chamber at −0.1 MPa for 4 h to evacuate the adsorbed moisture and gases from the surfaces of the biochars' pores. Subsequently, the biochar powder was blended with LA and maintained at 60 ℃ during agitation at a speed of 800 rpm for a duration of 3 h with the use of an automated hot plate magnetic stirrer. The process of mixing and stirring was conducted under constant vacuum conditions with a vacuum level of −0.1 MPa. Following 3 h of heating and stirring, the homogenous blend was kept on the filter paper inside vacuum oven to eliminate the spare fatty acid on the biochar surface. Eventually, the NB biochar shape stabilized PCMs were then obtained for further characterization. In this study, LA was impregnated into two different sets of

Table 1 Nomenclatures of the PCM composites with biochar to PCM ratios

Sample ID	Biochar	Biochar to LA weight ratio
NBL3-1	NB-300	2:1
NBL3-2	NB-300	1:1
NBL5-1	NB-500	1:1
NBL5-2	NB-500	1:2

biochars; NB-300 and NB-500. The quantities of LA and biochars with their naming conventions are presented in Table 1. Figure 1b presents a schematic representation of the synthesis process for shape-stabilized PCM.

2.3 Characterizations

2.3.1 CHNS analysis

The Neem seed biochar samples were analyzed with a CHNS analyzer (Thermo Scientific in Massachusetts, USA) to determine the levels of carbon, hydrogen, nitrogen, and sulfur in the samples.

2.3.2 Porosity and surface area analysis

The NB-300 and NB-500 biochar samples, as synthesized, were thoroughly characterized to assess their specific surface area and pore size distribution using a Brunauer–Emmett–Teller (BET) adsorption isotherm analyzer (Micromeritics 3Flex 5.01, Georgia, USA). The BET analysis was performed under controlled conditions, with the samples subjected to a temperature of 77 K. A relative pressure range of 0 to 1.0 was applied, ensuring accurate adsorption measurements. Prior to this, the samples underwent a degassing process for more than 12 h to remove any impurities, ensuring the reliability of the surface area and pore structure data obtained.

2.3.3 Electron microscopy

The shape and morphology of the synthesized biochars and biochar shape-stabilized PCMs were analyzed utilizing a Hitachi S-4800 field emission scanning electron microscope (FESEM) with an accelerating voltage of 15 kV. Platinum (Pt) coating was applied to the samples prior to the FESEM analysis. The biochar samples were also analyzed by energy-dispersive X-ray spectroscopy (EDS) equipped with FESEM.

2.3.4 Spectroscopy

FT-IR spectroscopy (Perkin Elmer UATR Two, United States of America) was used to analyze the chemical composition of biochar and shape-stabilized PCMs in the range of 500 to 4000 cm^{-1}.

2.3.5 Thermal examination

An in-depth thermal analysis was carried out using a differential scanning calorimeter (DSC; Q 20, TA Instruments) to comprehend the temperatures, enthalpies of phase transitions, and thermal cycle endurance. To assess the heat charging and discharging capabilities in DSC, a heating rate of 10 °C/min was utilized from 30 to 70 °C. A total of 500 thermal scans were performed within this temperature range, each utilizing the same heating and cooling rates, to evaluate the thermal cycle endurance. Moreover, thermogravimetric tests were carried out using a simultaneous thermal analyzer (STA 600, TA instruments), at a temperature span from 30 to 500 °C, with a heating rate of 10 °C/min. The onset temperatures of weight loss in the TGA curves were determined using the inbuilt software (TA Universal Analysis) in TA instruments by drawing two tangents at the slope transition regions; their point of intersection was taken as the onset of decomposition. All thermal analyses were conducted with a steady flow of N_2 gas at a rate of 20 ml/min. Standard aluminum and alumina pans were utilized for conducting DSC and TGA analyses, respectively. Before starting the thermal analyses, the instruments' enthalpy and temperature were calibrated using standard indium.

2.3.6 Leakage resilience

From an application perspective, it is essential for PCMs to have leakage resilience. To evaluate this characteristic, LA and shape stabilized PCM samples were placed onto Whatman filter papers and exposed to a hot plate for 60 min. The hot plate was adjusted to room temperature (25 °C) as well as 55 °C, which was higher than the melting point of LA. Observation of any soaking or staining on the filter papers indicated the presence of PCM leakage from the samples.

The thermal distribution of the samples was captured by an infrared (IR) thermal imaging (IR Camera, T250, Teledyne FLIR LLC, USA) every 5 minutes under controlled heating and cooling conditions.

3 Results and discussion

3.1 Pore structure

The N_2 adsorption–desorption isotherms of NB-300 and NB-500, measured using a BET analyzer at −196 ℃, are presented in Fig. 2, providing valuable insights into the textural properties, porosity, and adsorption behavior of these biochar samples, highlighting the effect of pyrolysis temperature on pore development. The NB-300 isotherm (Fig. 2a) exhibited a Type III profile, characteristic of materials with weak adsorbate-adsorbent interactions and predominantly macro/mesoporous structures (Ambroz et al. 2018; Bläker et al. 2019). The adsorption curve showed a slow and nearly linear increase

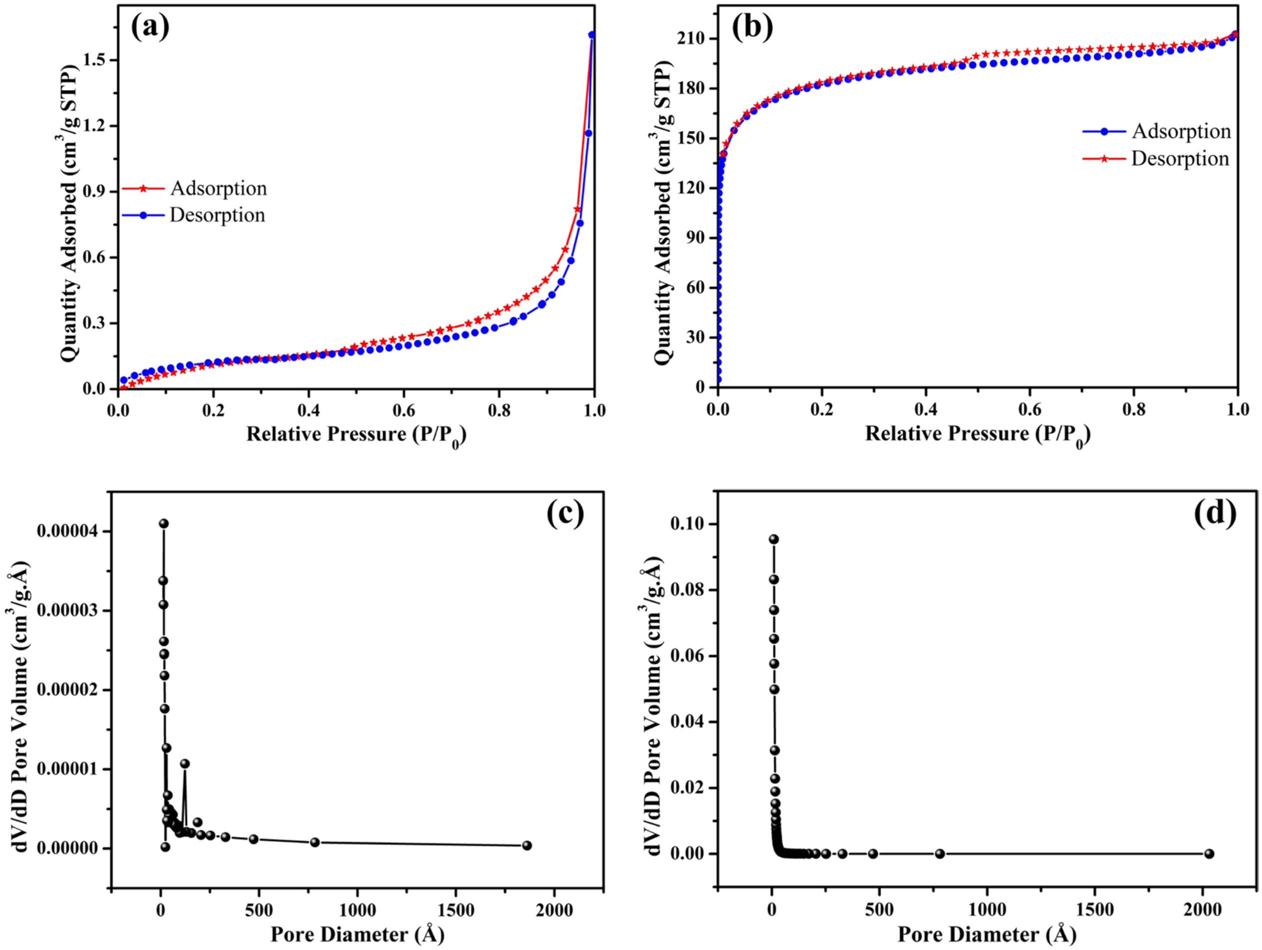

Fig. 2 N_2 sorption isotherms (− 196 ℃) of (**a**) NB-300, (**b**) NB-500; BJH pore size distribution plots of (**a**) NB-300, (**b**) NB-500

in nitrogen uptake across the relative pressure (P/P_0) range, indicating the dominance of multilayer adsorption rather than monolayer formation (Moodley et al. 2025). The lack of a steep rise at low P/P_0 (<0.1) confirms the absence of substantial microporosity, while a gradual uptake at higher P/P_0 (>0.8) suggests capillary condensation within larger mesopores and macropores. The absence of a significant hysteresis loop implies a non-rigid structure with minimal mesopore contribution. The BET surface area of NB-300 was 0.4819 m^2/g, reflecting extremely low porosity, and the BJH adsorption average pore width of 102.229 Å confirms a dominance of large mesopores (2–50 nm) (Mendoza et al. 2022), making it unsuitable for adsorption-driven applications. In contrast, the NB-500 isotherm (Fig. 2b) exhibited a Type IV profile, indicative of well-developed micromesoporosity, with a steep initial rise at low P/P_0 (<0.1), suggesting the presence of micropores. As P/P_0 increased, the adsorption curve gradually rose, followed by the emergence of a well-defined H4 hysteresis loop in the P/P_0 range of 0.4–1.0, confirming capillary condensation in slit-shaped mesopores typically found in layered materials (Bläker et al. 2019; Mandal et al. 2023b; Nkomo et al. 2021). The BET surface area of NB-500 was significantly higher at 668 m^2/g, indicating enhanced pore formation due to higher pyrolysis temperature, while the BJH adsorption average pore width of 14.630 Å placed it within the micropore range (<2 nm) (Mendoza et al. 2022). A comparative evaluation of NB-300 and NB-500 revealed that increasing the pyrolysis temperature from 300 ℃ to 500 ℃ resulted in a drastic transformation in porosity characteristics, with NB-300 exhibiting low surface area and a mesoporous structure due to incomplete devolatilization, while NB-500 endured extensive thermal degradation, leading to higher micropore and mesopore formation, increased surface area, and enhanced adsorption potential. The transition from a Type III to a Type IV isotherm, along with the appearance of an H4 hysteresis loop, demonstrated the evolution of pore structure, making NB-500 highly suitable for adsorption and energy storage applications, while NB-300 remained limited in utility due to its predominantly macro/mesoporous nature. Additionally, the pore size distribution plots of NB-300 and NB-500, illustrated in Fig. 2c and d, provided further confirmation of these structural differences, emphasizing the impact of pyrolysis temperature on biochar porosity.

To contextualize these results, Table 2 compares our data with literature-reported $ZnCl_2$-activated biochars derived from different biomasses. Reported BET surface areas range from ~214 m^2/g for sludge biomass (Minaei et al. 2023) to > 1600 m^2/g for Brazil nutshells (Lima et al. 2019), with pore volumes typically between 0.1 and 2.3 cm^3/g. These high values are often achieved using substantially higher $ZnCl_2$ dosages, frequently in the range of 1:1 to 1:8 biomass-to-$ZnCl_2$ by weight, which greatly enhances pore development. In contrast, the present study has employed an exceptionally low $ZnCl_2$ loading of 1:0.27, yet NB-500 still achieved a competitive surface area (668 m^2/g) relative to other moderate-temperature pyrolysis products such as orange peel biochar at 500 ℃ (700–1067 m^2/g; Saied et al. 2024) and grape waste biochar at 500 ℃ (912–1216 m^2/g) (Sayğılı et al. 2015). This demonstrates the efficiency of neem seed biomass in developing substantial surface area even under reduced chemical activation, which is advantageous from both an environmental and economic standpoint. Conversely, NB-300's very low surface area confirms that inadequate devolatilization at low pyrolysis temperatures limits the activation efficiency, regardless of the presence of $ZnCl_2$.

3.2 Functional group analysis

To understand the presence of functional groups after pyrolysis of NB, the biochar samples were analyzed through CHNS characterization. The respective weight percentages of carbon, hydrogen, nitrogen, and sulfur were found to be 33.20%, 2.57%, 1.08%, and 0.00% for NB-300 and 43.89%, 1.56%, 1.87%, and 0.00% for NB-500.

Furthermore, FT-IR analyses were carried out for both the biochars, and the FT-IR plot is presented in Fig. 3. Though the appearance and almost all the absorption peaks were visible in both the biochars, a few interesting differences were observed. Very diffuse absorption peaks at 3590 cm^{-1} were observed in both NB-300 and NB-500 samples, indicating the presence of hydroxyl groups in the biochar samples (Sánchez-Machado et al. 2024; Shukla 2024). The vibrational peaks appeared at 3450 and 1590 cm^{-1} are attributed to the stretching and bending of primary amines, respectively (Ariyanta et al. 2021; Grzelec 2024; Zakaria et al. 2024). The FTIR spectrum near 3016 cm^{-1} corresponds to the C–H stretching vibrations of aromatic compounds. The peak > 3000 cm^{-1} is commonly linked to the presence of alkanes and aliphatic compounds in the sample (Abdu et al. 2018; Ovchinnikov et al. 2016). The $-CH_3$ deformation vibration may produce a peak around 1434 cm^{-1}. This peak is typically associated with the bending or deformation modes of methyl ($-CH_3$) groups and can indicate the presence of various organic compounds, including alkanes and lipids (Gipson et al. 2015; Melo et al. 2013). Moreover, the FTIR peak near 2875 cm^{-1} corresponds to strong aliphatic C–H stretching vibrations. This indicates the presence of alkyl groups, suggesting that aliphatic hydrocarbons are part of the biochar structure (Abdeen et al. 2023; Fu et al. 2016).

The vibrational peak observed at 1740 cm^{-1} corresponds to the stretching vibration of the carbonyl (C=O) bond. This peak is characteristic of functional groups such as esters, aldehydes, ketones, and carboxylic acids, indicating the presence of carbonyl-containing compounds in the sample (Gurav et al. 2022; Thongsamer et al. 2022). Additionally, the absorption peak at 1028 cm^{-1} is attributed to the C=O stretching vibrations (Choi et al. 2020; Siipola et al. 2018) of carboxylic, ester, and ether groups, commonly found in cellulose and hemicellulose whereas the peak at 1090 cm^{-1} is attributed to the bending of C–O (Wang et al. 2018; Zou et al. 2024b). The peak observed at 1369 cm^{-1} is attributed to the presence of acidic functional groups, specifically from carboxylic and phenolic groups. Additionally, the absorption peak at 1216 cm^{-1} indicates the presence of amine groups (Thongsamer et al. 2022). The peak found at 2142 cm^{-1} is associated with the stretching of C≡C bonds in alkynes present in hemicellulose, and becomes more prominent after pyrolysis at the higher temperature (Armynah et al. 2019).

The absorption peaks at 770 and 905 cm^{-1} are associated with the out of plane bending vibration of C–H aromatic ring and O–H groups (Cole et al. 2019; Dehkhoda et al. 2014). The Zn–OH stretching and bending modes are the cause of the peak seen at 600 cm^{-1} in the NB-500 sample (Shankar and Rayappan 2017). Though the biochars were cleaned thoroughly with distilled water, the appearance of peaks related to Zn–OH is due to the activation of biochars with $ZnCl_2$ before pyrolysis, which at higher temperature has resulted in the formation of $Zn(OH)_2$.

3.3 Microscopic investigation of biochars

The morphological and elemental characteristics of biochar play a crucial role in determining its suitability for PCM stabilization, as these properties directly influence the material's adsorption capacity, thermal stability, and overall performance in composite systems. FE-SEM analysis of NB-300 (Fig. 4a) and NB-500 (Fig. 5a) biochars

Table 2 Comparison of the pore morphology data with reported values of different $ZnCl_2$-activated biochars from various biomass precursors

No	Biomass	Temperature (℃)	Biomass to $ZnCl_2$ ratio	BET surface area (m^2/g)	Total pore volume (cm^3/g)	Pore diameter (nm)	Ref
1.	Sludge biomass	Microwave (2.45 GHz)	1:3.4	214	0.127	0.012	(Minaei et al. 2023)
2.	Buriti shells	700	1:3	843	0.490	2.32	(Pezoti Jr et al. 2014)
3.	Pine sawdust	850	1:4	471.4	0.26	< 2 nm	(Pimentel et al. 2023b)
4.	Pine sawdust	850	1:4	501.1	0.26	< 1 nm	(Pimentel et al. 2023a)
5.	Carrot juice pulp and pomegranate peel	Microwave at 600 W	2:1	1202.2	0.703	3.0	(Suhaimi et al. 2022)
6.	Mixture of orange peel and watermelon rind	Microwave at 800 W	1:2	661.3	0.49	4.57	(Hanafi et al. 2024)
7.	Cocos nucifera shells	550	1:1	544	–	–	(Sangeetha Piriya et al. 2021)
8.	Tomato processing solid waste	500	1:1	617	0.437	2.64	(Sayğılı and Güzel 2016)
9.	Tomato processing solid waste	500	1:2	722	0.457	4.49	(Sayğılı and Güzel 2016)
10.	Tomato processing solid waste	500	1:4	760	0.710	4.83	(Sayğılı and Güzel 2016)
11.	Tomato processing solid waste	500	1:6	787	1.000	5.78	(Sayğılı and Güzel 2016)
12.	Tomato processing solid waste	500	1:8	495	0.452	3.65	(Sayğılı and Güzel 2016)
13.	Tomato processing solid waste	400	1:6	648	0.756	4.56	(Sayğılı and Güzel 2016)
14.	Tomato processing solid waste	600	1:6	1093	1.569	5.92	(Sayğılı and Güzel 2016)
15.	Tomato processing solid waste	800	1:6	492	0.106	2.41	(Sayğılı and Güzel 2016)
16.	Cotton waste denim	500	1:1	490	0.812	–	(Zhang et al. 2023)
17.	Biogas residue	700	1:1	516.67	0.243	12.63	(Xia et al. 2016)
18.	Corn cobs	700	2:1	1201.1	0.590	1.73–4.27	(Varela et al. 2024)
19.	Orange peel	500	1:1	700	0.642	–	(Saied et al. 2024)
20.	Orange peel	500	1:2	906	0.8	–	(Saied et al. 2024)
21.	Orange peel	500	1:3	1067	1.29	–	(Saied et al. 2024)
22.	Orange peel	500	1:4	825	0.74	–	(Saied et al. 2024)
23.	Tobacco	750	1:1.36	479.4	0.06	–	(Celso Goncalves et al. 2022)
24.	Brazil nutshells	600	1:1	1457	0.666	≤ 1.1	(Lima et al. 2019)
25.	Brazil nutshells	600	1:1.5	1640	0.929	< 1	(Lima et al. 2019)
26.	Grape waste	500	1:1	912	0.608	2.40	(Sayğılı et al. 2015)
27.	Grape waste	500	1:2	1015	0.630	2.76	(Sayğılı et al. 2015)
28.	Grape waste	500	1:4	1216	1.862	6.02	(Sayğılı et al. 2015)
29.	Grape waste	400	1:6	819	0.556	2.71	(Sayğılı et al. 2015)
30.	Grape waste	500	1:6	1361	2.000	6.33	(Sayğılı et al. 2015)
31.	Grape waste	600	1:6	1455	2.318	6.81	(Sayğılı et al. 2015)
32.	Grape waste	800	1:6	988	0.984	3.96	(Sayğılı et al. 2015)
33.	Aerobic granular sludge	700	1:6.8	852.41	0.086	2.46	(Yan et al. 2020)
34.	Spent coffee grounds	550	1:2	305.20	–	2.743	(Sharma et al. 2024)
35.	Spent coffee grounds	750	1:2	720.52	–	2.405	(Sharma et al. 2024)
36.	Neem seeds	300	1:0.27	0.4819	0.003	10.23	This study
37.	Neem seeds	500	1:027	668	0.445	1.463	This study

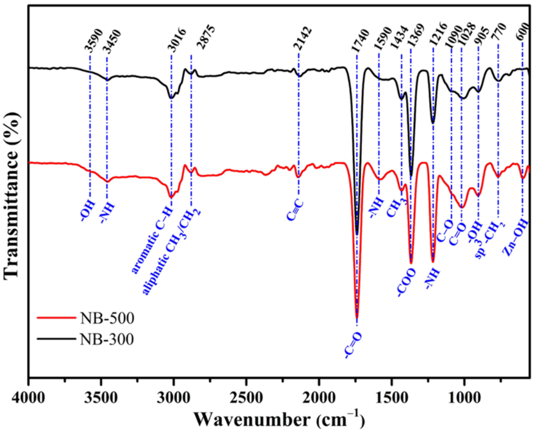

Fig. 3 FTIR spectra of NB-300 and NB-500 biochar samples

revealed a well-developed porous structure with interconnected channels, which provided a high surface area and facilitated the effective accommodation of PCMs within the biochar matrix. Notably, the pores in NB-500 biochar were significantly larger and more prominent compared to those in NB-300, suggesting that higher pyrolysis temperatures contribute to enhanced porosity. This increased pore size and volume in NB-500 can significantly improve PCM accommodation and distribution within the biochar, minimizing leakage and enhancing thermal stability.

Furthermore, EDS results presented in Table 3 indicate notable compositional changes with increasing pyrolysis temperature. The elemental mapping results provided qualitative distributions of key elements, including carbon (C), nitrogen (N), oxygen (O), phosphorus (P), sulfur (S), silicon (Si), zinc (Zn), and chlorine (Cl). The EDS mappings for individual elements are illustrated in Figs. 4b–i and 5b–i) for NB-300 and NB-500, respectively. The carbon content increased from 50.64 mass% in NB-300 to 69.28 mass% in NB-500, which reflects a higher degree of carbonization and structural integrity. Simultaneously, oxygen and silicon contents decreased from 22.48 to 8.24 mass% and from 2.54 to 0.24 mass%, respectively, due to the thermal degradation of oxygen-containing functional groups. This reduction in oxygen content leads to a more hydrophobic biochar surface, which can improve PCM compatibility and prevent undesirable interactions with moisture. The significant reduction in silicon content from NB-300 to NB-500 can be attributed to post-pyrolysis washing with deionized

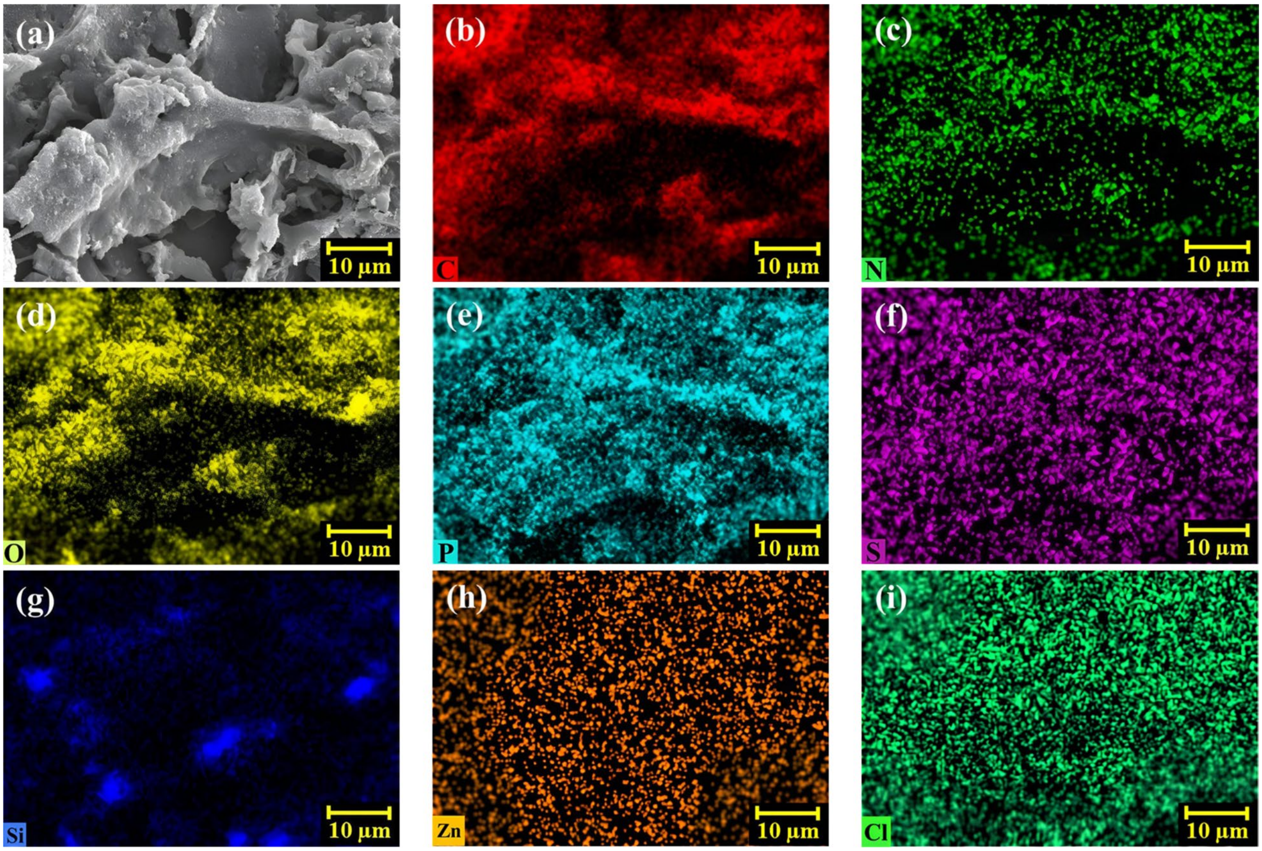

Fig. 4 **a** SEM and (**b**–**i**) elemental distribution of C, N, O, P, S, Si, Zn, and Cl in NB-300 sample by EDS mapping

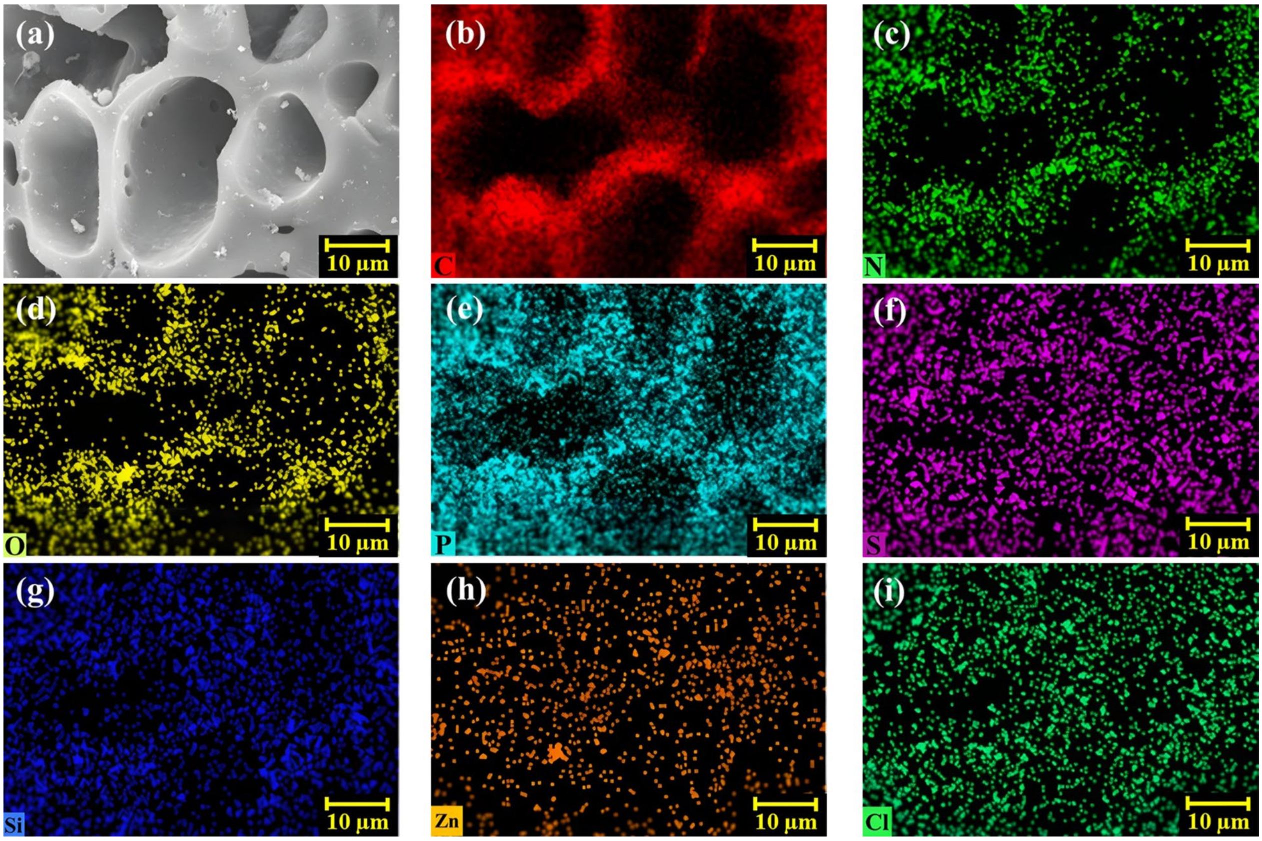

Fig. 5 (**a**) SEM and (**b**–**i**) elemental distribution of C, N, O, P, S, Si, Zn, and Cl in NB-500 sample by EDS mapping

water, which likely removed surface-bound inorganic residues. Additionally, higher pyrolysis temperatures may lead to partial volatilization or deeper diffusion of silicon species, making them less detectable by EDS. The increased carbon content at elevated temperatures also contributes to a relative decrease in detectable silicon. Phosphorus and sulfur remained relatively stable, suggesting that these elements provide additional structural stability to the biochar. Additionally, the nitrogen content increased significantly from 8.00 to 14.90 mass%, indicating a higher presence of nitrogen-containing functional groups, such as amines, which are reported to enhance interfacial interactions between the biochar and adsorbates (Bachs-Herrera et al. 2024; Petrovic et al. 2022; Pietrzak 2009). This observation aligns with the FTIR analysis, which detected a higher concentration of amine groups in the NB-500 biochar sample. However, the discrepancy between nitrogen content values obtained by EDS and CHNS analysis is due to differences in their analytical principles. CHNS is a bulk method providing accurate quantification of C, H, N, and S, whereas EDS is a semi-quantitative, surface-sensitive technique prone to variability for light elements like nitrogen. Therefore, CHNS values are considered more reliable and used for nitrogen quantification in this study.

The improved porosity, increased carbonization, and enriched functional groups in NB-500 collectively enhanced the structural integrity, adsorption capability, and might be potential for interfacial bonding of the biochar-PCM composite. These characteristics might lead to improved thermal performance, reduced leakage, and prolonged operational stability.

Although additional pyrolysis was carried out at 750 °C and 1000 °C, the resulting biochars exhibited reduced BET surface areas (186 m^2/g and 356 m^2/g, respectively), minimal surface functionality, and poor mechanical integrity. These limitations rendered them unsuitable for effective PCM shape stabilization. Intermediate temperatures such as 400 °C and 600 °C were not examined in detail in this study due to experimental resource constraints and because preliminary results, along with literature evidence (Elnour et al. 2019; Janu et al. 2021), suggested their performance would fall between that of 300 °C and 500 °C without offering distinct advantages. Consequently, the study focused on biochars prepared at 300 °C and 500 °C, which provided the optimal

Table 3 Mass% and atom% from elemental analysis of biochars by EDS

Biochar	Element	C	N	O	Si	P	S	Cl	Zn
NB-300	Mass (%)	50.64	8.00	22.48	2.54	4.66	0.19	2.58	8.92
	Atom (%)	63.42	8.59	21.13	1.36	2.26	0.09	1.10	2.05
NB-500	Mass (%)	69.28	14.90	8.24	0.24	3.68	0.41	0.37	2.88
	Atom (%)	76.48	14.10	6.83	0.11	1.58	0.17	0.14	0.58

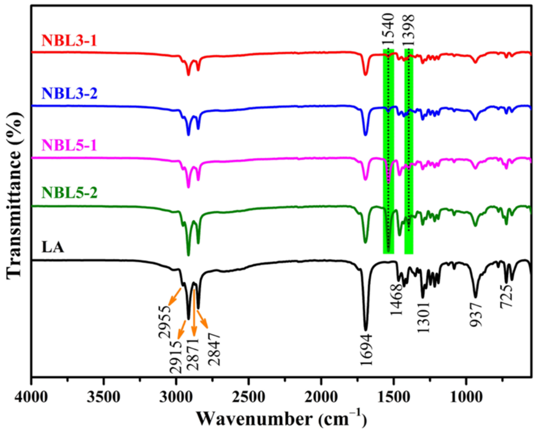

Fig. 6 FTIR spectra of pure LA, and LA impregnated biochar PCM composites

combination of structural integrity, surface functionality, and textural properties for the intended application.

3.4 FTIR analysis of the PCM-impregnated biochar composites

The FTIR spectroscopic analysis was further conducted on pure LA as a reference and LA-impregnated NBL3 and NBL5 biochar-based PCM composites, with the results presented in Fig. 6. The spectral analysis revealed the presence of six prominent absorption peaks for pure LA at 2915, 2847, 1694, 1301, 937, and 725 cm^{-1}, accompanied by three additional minor peaks at 2955, 2871, and 1468 cm^{-1}. The emergence of these peaks is attributed to the characteristic vibrational modes of three principal functional groups present in LA: alkyl ($-CH_3$ and $-CH_2$), carboxyl ($-COO^-$), and hydroxyl ($-OH$) (Mandal et al. 2022a). The peaks at 2955 cm^{-1} and 2915 cm^{-1} are associated with the asymmetric stretching vibrations of methyl ($-CH_3$) and methylene ($-CH_2$) groups, respectively, whereas their symmetric stretching modes are responsible for the absorption bands observed at 2871 cm^{-1} and 2847 cm^{-1} (Mandal et al. 2023b; Sharifah et al. 2017). A distinct and intense peak at 1694 cm^{-1} corresponds to the C=O stretching vibration of the carboxyl functional group in LA (Ishak et al. 2021a). Furthermore, a minor absorption peak at 1468 cm^{-1} is attributed to the presence of a methylene ($-CH_2$) bridge, confirming the aliphatic nature of the molecule (Mandal et al. 2022b).

Additional absorption features included a weak peak at 1301 cm^{-1}, which corresponds to the O–C stretching vibration, and another at 725 cm^{-1}, attributed to the C–H plane bending vibration (Ishak et al. 2021a; Yanghua et al. 2020). The presence of a peak at 937 cm^{-1} indicates an out-of-plane bending vibration associated with hydroxyl ($-OH$) functional groups (Mandal et al. 2022b; Zhang et al. 2019).

Upon impregnation of LA into biochar-based PCM composites, the same characteristic peaks of LA were observed, suggesting that the core molecular structure of LA remained intact within the composite matrix. However, an evident increase in the intensities of these peaks was recorded with higher LA loading. Besides, an interesting observation can be seen in the emergence of two new peaks at 1540 and cm^{-1} and 1398 cm^{-1} after the impregnation of LA into the biochars. However, the detectable peak intensities at 1540 cm^{-1} were very low in the case of NBL3-1 and NBL3-2 PCM composites, while they were very high in NBL5-1 followed by NBL5-2. Another peak at 1398 cm^{-1} was not visible in the case of NBL3-1 and NBL3-2 PCM composites. As reported by Xing et al., N–H deformation for amide II at around 1540 cm^{-1}, C–N stretching for amide II at around 1398 cm^{-1} result in the formation of these two peaks (Xing et al. 2015). The absence of the 1398 cm^{-1} peak in the NBL3-1 and NBL3-2 PCM composites suggests a lack of or significantly reduced presence of the functional groups responsible for this vibrational mode. In the case of NBL5-based composites, where biochar was synthesized at higher pyrolysis temperatures, a higher nitrogen content was observed through FTIR and EDS analysis. This likely facilitates the formation of amide-like interactions, leading to the appearance of both 1539 cm^{-1} (N–H deformation) and 1398 cm^{-1} (C–N stretching) peaks. Conversely, in the NBL3-based composites, produced at a lower pyrolysis temperature, nitrogen functionalization appeared to be lower, preventing the formation of the 1398 cm^{-1} peak.

The absence of this peak in NBL3-1 and NBL3-2 further suggests that nitrogen-related functionalities, particularly

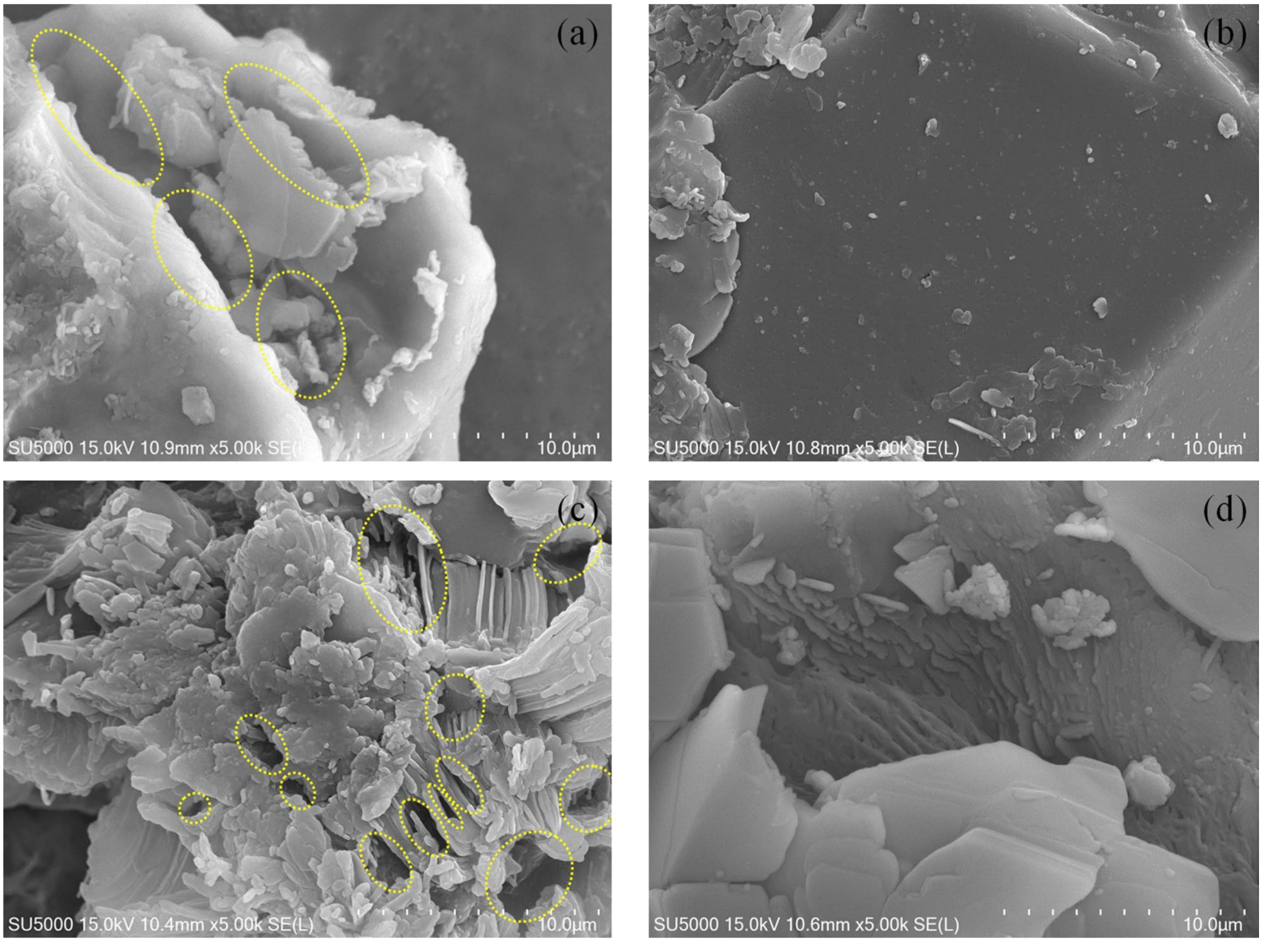

Fig. 7 SEM micrographs after PCM impregnation (**a**) NBL3-1, (**b**) NBL3-2, (**c**) NBL5-1, and (**d**) NBL5-2

amide II structures, are not significantly involved in PCM stabilization within these composites.

3.5 *Morphological analysis of PCM-impregnated biochar composites* via *FE-SEM*

The morphological characteristics of the PCM-impregnated biochar composites were analyzed using FE-SEM, and the corresponding micrographs are presented in Fig. 7a–d. The SEM images of the as-received biochars (Fig. 4a and Fig. 5a) revealed a well-defined porous structure with interconnected channels, which serve as potential sites for PCM accommodation. Upon impregnation with lauric acid (LA), a significant morphological transformation was observed, as the previously open pores and channels became occupied by the phase change material. In the case of NBL3-1 (Fig. 7a) and NBL5-1 (Fig. 7c), a few unfilled pores remained visible (highlighted with yellow circles), indicating an incomplete infiltration of LA due to inadequate PCM loading. Interestingly, while the NBL3-1 sample exhibited fewer visible unfilled pores than NBL5-1, the size of the unfilled voids in NBL3-1 was significantly larger, suggesting that the lower porosity and structural properties of NB-3 biochar limited complete PCM penetration at this loading ratio. Conversely, in NBL5-1, although the number of unfilled pores was greater, they were much smaller in size, which can be attributed to the higher porosity and greater PCM-holding capacity of NB-5 biochar.

At higher LA loading levels (NBL3-2 and NBL5-2, Fig. 7b and d), no unfilled pores were detectable. This observation suggests that NB-5 biochar can accommodate nearly double the mass of LA compared to NB-3 biochar, reinforcing its superior suitability as a PCM carrier. The optimized 1:1 and 1:2 biochar-to-LA ratios for NB-3 and NB-5, respectively, ensured full pore saturation, preventing PCM leakage and enhancing composite stability. This trend was further corroborated by TGA and DSC data, which showed no significant changes in thermal behavior beyond the critical biochar-to-LA loading ratios. Consequently, PCM composites exceeding the optimized biochar-to-PCM ratios were excluded from this study, as additional biochar content beyond the

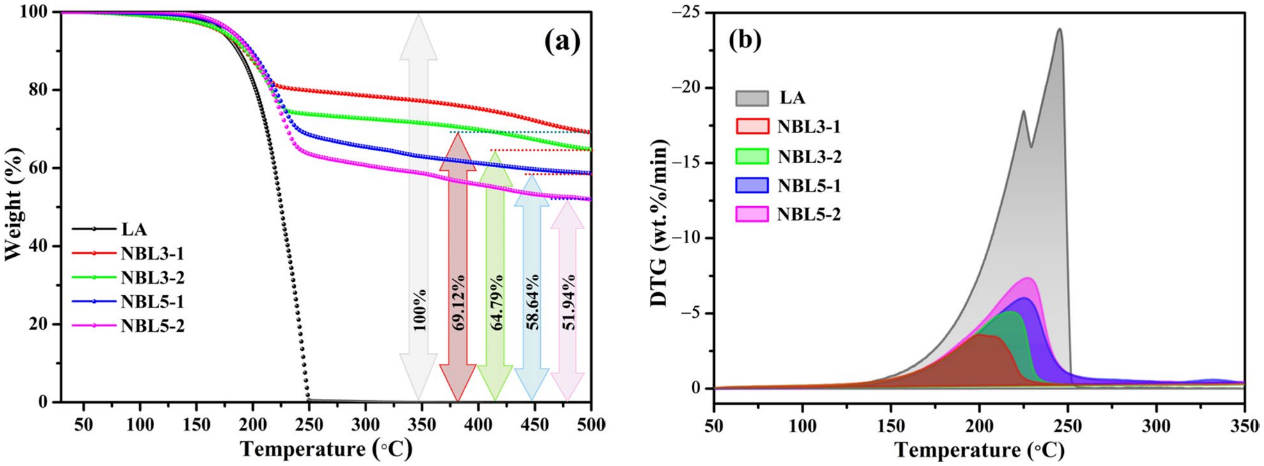

Fig. 8 (**a**) TGA and (**b**) DTG thermograms of LA and synthesized PCM composites

saturation point does not contribute to improved thermal performance.

3.6 Thermal stability analysis of PCM-impregnated biochar composites

The thermal stability of the synthesized biochar-PCM composites was assessed using thermogravimetric analysis (TGA), and the corresponding thermograms are compared with pure LA in Fig. 8a. To further interpret the gravimetric data, the differential thermogravimetric (DTG) curves are also presented in Fig. 8b. The TGA results clearly indicate that pure LA endured complete weight loss beyond 250 °C, signifying its full decomposition at higher temperatures. However, in the case of biochar-PCM composites, significant weight retention was observed due to the encapsulation of LA within the porous biochar structure. The recorded residual weights for NBL5-1 and NBL5-2 were 48.06% and 41.36%, respectively, while NBL3-2 and NBL3-1 exhibited 35.21% and 30.88% weight losses, respectively. In the TGA plot, the weight loss percentages are indicated.

A notable observation arises from the onset temperature of weight loss, which signifies the thermal degradation threshold of the materials. The highest onset temperature was recorded for NBL5-2 at 156.75 °C, followed by NBL5-1 (155.38 °C), NBL3-2 (149.14 °C), NBL3-1 (147.71 °C), and pure LA (138.67 °C). These results confirmed that PCM impregnation into biochar significantly enhanced thermal stability, particularly in NB-5 biochar-based composites, which outperformed their NB-3 counterparts. Furthermore, all the samples exhibited superior thermal stability up to 125 °C, with no detectable weight loss in this temperature range, demonstrating their suitability for TES applications within moderate temperature regimes.

The increased thermal stability in the biochar-PCM composites can be attributed to the encapsulation of PCM molecules within the biochar pores and channels, where they interact with surface functional groups as seen in the FTIR results of the biochar PCM composites (Sect. 3.4). These intermolecular interactions, including hydrogen bonding, van der Waals forces, and capillary action, help to stabilize the LA molecules, reducing easy volatilization and decomposition at elevated temperatures. Additionally, CHNS, FTIR, and EDS analyses revealed that NB-5 biochar contained a higher concentration of nitrogen-containing functional groups, which likely contribute to stronger interfacial interactions with LA. This may explain the superior thermal stability observed in NBL5-1 and NBL5-2 composites compared to their NB-3 counterparts. These findings highlight the critical role of biochar structure and surface chemistry in enhancing PCMs' thermal stability.

3.7 Thermal energy storage capability

The evaluation of heat storage capability is a critical determinant in assessing the suitability of PCMs for TES applications. Key thermal parameters, including enthalpies of phase transition (ΔH_m, ΔH_s) and transition temperatures (T_m and T_s), were precisely analyzed using DSC during both the melting and solidification processes. The thermal characteristics, systematically documented in Table 4, offer profound insights into the heat storage and release behavior of the synthesized biochar PCM composites. The DSC thermograms for heating and cooling cycles are presented separately in Figs. 9a and b, respectively. From the DSC thermograms, it is evident that all PCM composites exhibited distinct and well-defined single melting and solidification peaks. As expected, pure LA exhibited the highest

Table 4 Thermal parameters of melting and solidification of the synthesized PCM composites

Sample	$T_{m\,(onset)}$ (℃)	$T_{m\,(peak)}$ (℃)	ΔH_m (J/g)	$T_{s\,(onset)}$ (℃)	$T_{s\,(peak)}$ (℃)	ΔH_s (J/g)	R_s
LA	44.91	47.57	186.41	40.27	42.03	185.76	–
NBL3-1	44.32	47.60	55.11	38.84	40.48	54.71	29.56
NBL3-2	43.96	47.65	64.29	39.20	40.86	63.26	34.49
NBL5-1	43.92	47.63	77.15	39.27	41.38	75.97	41.39
NBL5-2	44.10	50.02	94.92	37.30	41.44	92.16	50.92

melting (ΔH_m) and solidification (ΔH_s) enthalpies, measured at 186.41 J/g and 185.76 J/g, respectively. Among the biochar PCM composites, NBL5-2 displayed the highest enthalpy values, with ΔH_m and ΔH_s recorded at 94.92 J/g and 92.16 J/g, respectively, followed by NBL5-1 (77.15 J/g and 75.97 J/g), NBL3-2 (64.29 J/g and 63.26 J/g), and NBL3-1 (55.11 J/g and 54.71 J/g). The higher enthalpy values observed in NBL5-1 and NBL5-2 were well corroborated by their enhanced porosity, as verified by BET surface area analysis and SEM imaging. Since NB-5 biochar exhibited a higher degree of porosity compared to NB-3 biochar, it facilitated the accommodation of a greater amount of LA, thereby enhancing the overall thermal storage capacity. This observation aligns with the well-established structure–property relationship, which suggests that higher pyrolysis temperatures yield biochar with increased porosity, thereby allowing for a greater degree of PCM impregnation and, consequently, a progressive increase in enthalpy values with increasing PCM loading.

Regarding phase transition temperatures, the highest melting peak temperature ($T_{m\,(peak)}$) was recorded at 50.02 ℃ for NBL5-2, whereas pure LA exhibited the lowest $T_{m\,(peak)}$ at 47.57 ℃. Although no obvious trend in $T_{m\,(peak)}$ is observed, the elevation in $T_{m\,(peak)}$ across the biochar composites can be attributed to the previously discussed physical interactions (Sect. 3.6), including surface tension effects, capillary forces, spatial confinement within biochar pores, van der Waals interactions, and interfacial bonding between PCM molecules and biochar functional groups (Sect. 3.4). Notably, NBL3-2 and NBL5-2 exhibited higher $T_{m\,(peak)}$ values than their respective counterparts (NBL3-1 and NBL5-1), which can be attributed to their higher PCM uptake, leading to enhanced molecular entrapment within the biochar matrix. The higher accommodations of LA in the confined spaces in pores and channels led to the retardation of molecular movement, thereby delaying the melting.

During solidification, phase transition behavior followed a similar trend. From the solidification curves in Fig. 9b, it can be seen that pure LA exhibited noticeable supercooling during the cooling cycle in the DSC scan. This phenomenon was characterized by a significant delay in crystallization onset, leading to a discrepancy between melting and solidification patterns. However,

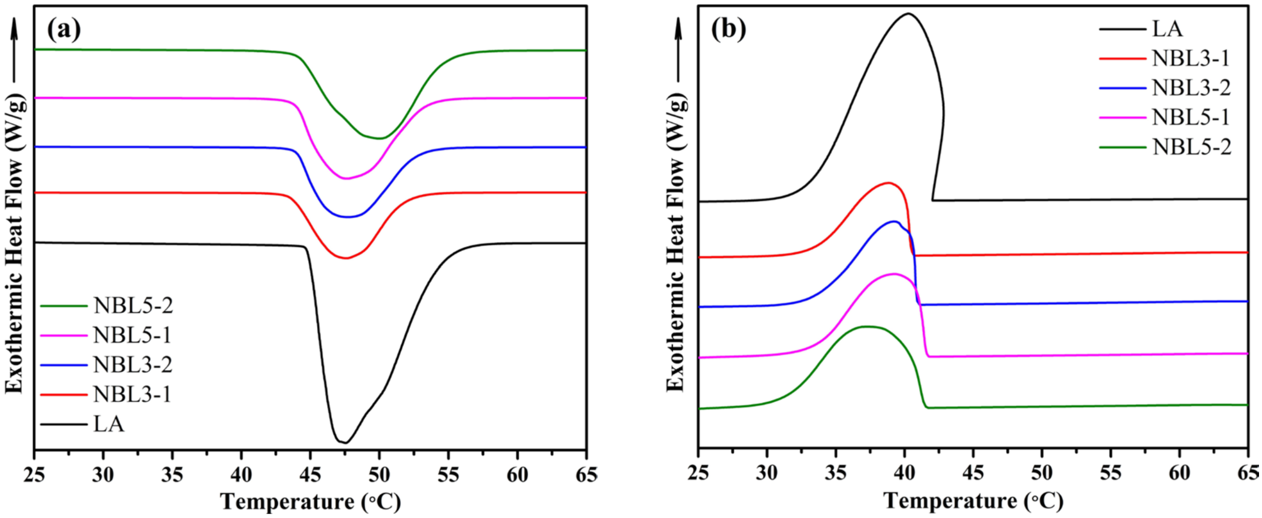

Fig. 9 Heating (**a**) and cooling (**b**) curves obtained from the DSC scans

the supercooling tendency of LA was effectively suppressed through shape stabilization with biochar. The onset solidification temperature ($T_{s\ (peak)}$) was found to be highest for pure LA (40.27 ℃), while the lowest was observed for NBL5-2 (37.30 ℃). The lower T_s, onset in biochar stabilized PCMs suggests an extended subcooling effect, which may be attributed to restricted molecular mobility and enhanced intermolecular interactions between PCM molecules and biochar functional groups.

The restricted molecular mobility of LA within the narrow, confined spaces of biochar pores and channels induced a delayed phase transition, contributing to an overall increase in the melting temperature. Despite the larger pore structures in NB-5 biochar, the higher presence of nitrogen-containing functional groups (as corroborated by FTIR and EDS analysis) enhanced molecular stabilization through hydrogen bonding and electrostatic interactions, further reinforcing the PCM retention within the biochar framework. This molecular stabilization mechanism is equally applicable to the solidification process, where phase transition is delayed (towards lower temperatures) due to physical and chemical interactions contributing to an optimized thermal response. This enhanced thermal storage and release behavior ensures superior phase transition stability, rendering biochar-stabilized PCMs highly suitable for diverse TES applications.

To further quantify the shape stabilization efficacy of the biochar-PCM composites, the shape stabilization ratio (R_s) and heat storage efficiency (E_s) were systematically computed and were documented in Table 4. The R_s values were calculated from the enthalpy data obtained from DSC scans using Eq. (1) (Ma et al. 2024; Patel et al. 2023; Yan et al. 2024).

$$R_s = \frac{\Delta H_{m(PCMcomposite)}}{\Delta H_{m(LA)}} \times 100 \tag{1}$$

where melting enthalpies of shape-stabilized PCM composites and LA are denoted by the $\Delta H_{m,\ PCM\ Composite}$, $\Delta H_{m,\ LA}$, respectively. The R_s values for NBL3-1, NBL3-2, NBL5-1, and NBL5-2 are determined to be 29.56, 34.49, 41.39, and 50.92, respectively, exhibiting a progressive increase with enhanced porosity and specific surface area of the biochar matrix. This observed trend aligns precisely with the SEM and BET surface area analysis, validating that higher porosity and larger pore diameter contribute significantly to the superior shape stabilization ratio (R_s) in NBL5 PCM composites. The enhanced microporous and mesoporous structure of NB-5 biochar, achieved through higher pyrolysis temperatures, facilitates an increased PCM retention capacity by effectively confining LA molecules within the intricate pore network. Moreover, the R_s and E_s values strongly corroborate the TGA results, in which the LA loading within the biochar matrix is evidenced by the weight loss percentages observed during thermal degradation. These findings further substantiate that higher PCM retention within biochar pores enhances thermal stability and phase transition efficiency, indicating that biochar structure plays a pivotal role in optimizing thermal energy storage performance.

Previous research on biochar-based shape-stabilized PCM composites remains limited. Wan et al. reported the highest R_s value of 38.58 for palmitic acid impregnated into Pinus cone biochar (Wan et al. 2019). Similarly, an almond shell biochar-stabilized polyethylene glycol PCM composite exhibited an R_s value of 43.76 (Chen et al. 2018). The R_s value for myristic acid incorporated into orange peel biochar was reported as 39.6 (Mandal et al. 2022b). Moreover, wheat straw biochar to eicosane at a 2:1 ratio has achieved an R_s of 37.1 (Atinafu et al. 2021). Rice husk biochar-stabilized palm wax was demonstrated an R_s value of 50.1 (Jeon et al. 2019). The R_s value of 1-decanol shape-stabilized with oilseed rape biochar was reported at 38.4, while sewage sludge biochar-stabilized n-dodecane and 1-dodecanol showed R_s values of 36.0 and 29.3, respectively (Atinafu et al. 2020). Carbonized pepper straw-stabilized palmitic acid exhibited an R_s value of 45.41 (Gu et al. 2019). The R_s value for hazelnut wood biochar-stabilized capric acid was reported as 51.60 (Hekimoğlu et al. 2021). Additionally, coconut shell charcoal impregnated with stearic acid under various activation conditions displayed R_s values of 14.61, 24.83, 29.78, and 34.58 (Xie et al. 2020a). Corn straw biochars pyrolyzed at 400, 500, 600, and 800 ℃ were reported to shape-stabilize polyethylene glycol (PEG) with R_s values 49.28, 40.23, 46.84, and 36.02, respectively (Liu et al. 2022). Furthermore, carbonized potato (CP) shape-stabilized PEG at 1:3, 1:2, 1:1.5, and 1:1 PEG-to-CP ratios resulted in R_s values of 25.85, 34.02, 40.54, and 50.05, respectively (Tan et al. 2016).

The Rs and ΔH_m values obtained in this study were compared with literature data and are presented in Fig. 10. The results demonstrated that the Rs values of the tested biochar-based phase-stabilized composites were comparatively superior and align well with previously reported values. Notably, the highest Rs value (50.92) was observed in the NBL5-2 composite. The synthesized PCM composites exhibited superior thermal stability, structural integrity, and enhanced latent heat storage capacity, making them highly suitable for applications in TES, such as energy-efficient buildings, electronic cooling systems, and renewable energy storage solutions. These biochar-based composites offer a sustainable and cost-effective alternative to conventional phase change materials, contributing to improved energy efficiency and

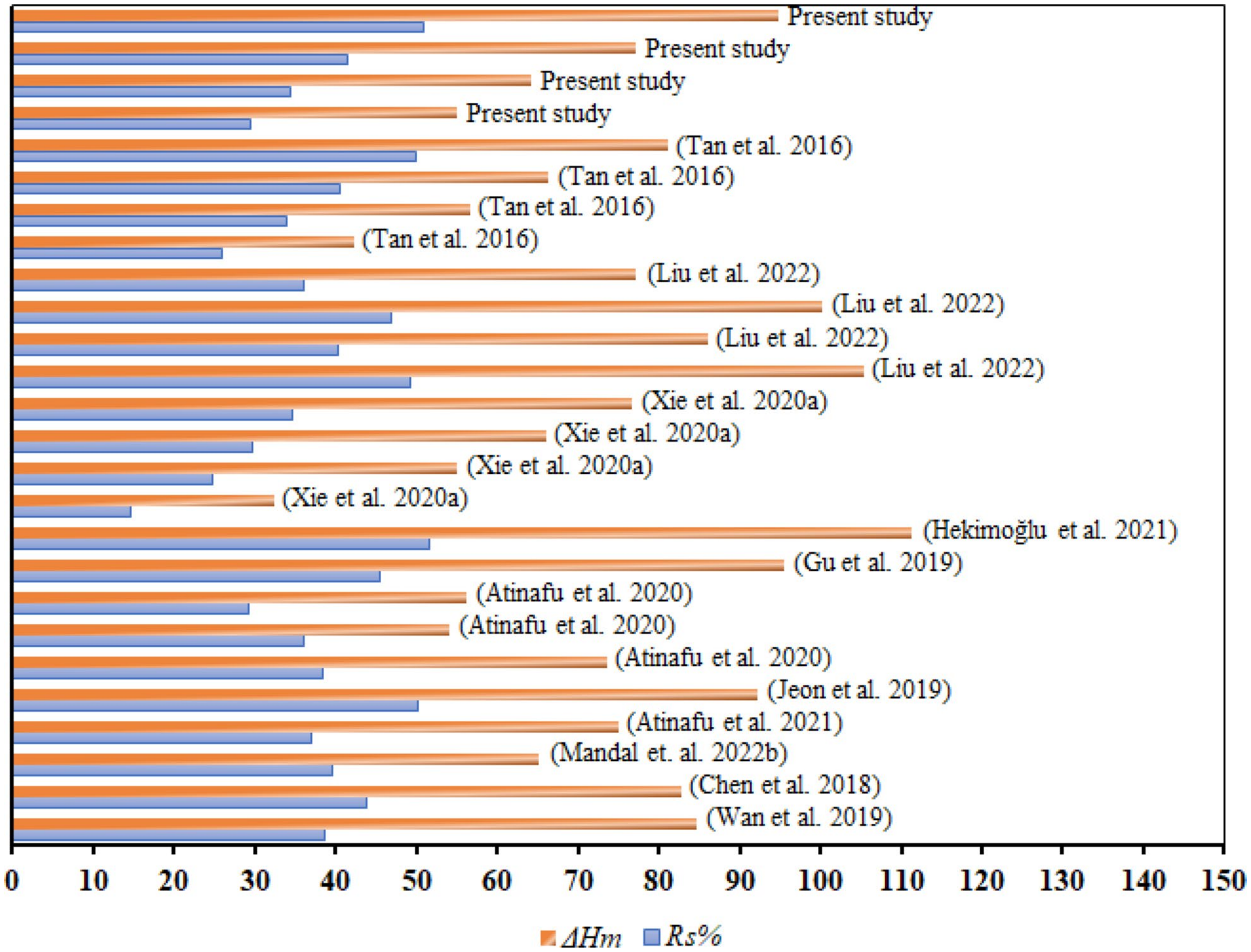

Fig. 10 Comparison of obtained R_s and ΔH_m values with reported data for various biochar-based phase-stabilized composites from literature

environmental sustainability across various industrial and commercial sectors.

3.8 Heat charging-discharging congruencies

Thermal stability, particularly with regard to heat charging and discharging congruency, is a pivotal determinant of a phase change material (PCM) composite's longevity and reliability over prolonged operational durations. To methodically assess this stability, differential scanning calorimetry (DSC) analyses were conducted over 500 successive thermal cycles in an isochronal mode, employing a heating rate of 10 °C/min with an isothermal holding period of 3 min before each heating and cooling segment. The DSC thermograms, illustrating the thermal cycling behavior of NBL3-2 and NBL5-2 composite PCM samples, are depicted in Figs. 11a and b, where only the first and every 50th cycles are represented for clarity and conciseness.

A meticulous examination of the heat charging and discharging profiles revealed the presence of distinct single endothermic and exothermic peaks, corresponding to melting (T_m) and solidification (T_s), respectively. Notably, throughout the entire 500-cycle duration, no substantial deviations in the characteristic peak temperatures were discernible, indicating the composites' robust thermal stability. However, a gradual and marginal decline in enthalpy values was observed across both heating and cooling segments for both samples, indicative of slight thermal degradation or material fatigue. The extracted enthalpy values for the first cycle and every 50th cycle of heating and cooling, along with the corresponding enthalpy retention percentages, are systematically compiled in Figs. 11c and d for NBL3-2 and NBL5-2, respectively.

For the NBL3-2 composite PCM, the melting enthalpy decreased from 64.29 J/g to 63.31 J/g over 500 cycles, while the solidification enthalpy declines from 63.26 J/g to 62.2 J/g. In contrast, the NBL5-2 composite PCM demonstrated even greater thermal resilience, with melting enthalpy decreasing marginally from 94.92 J/g

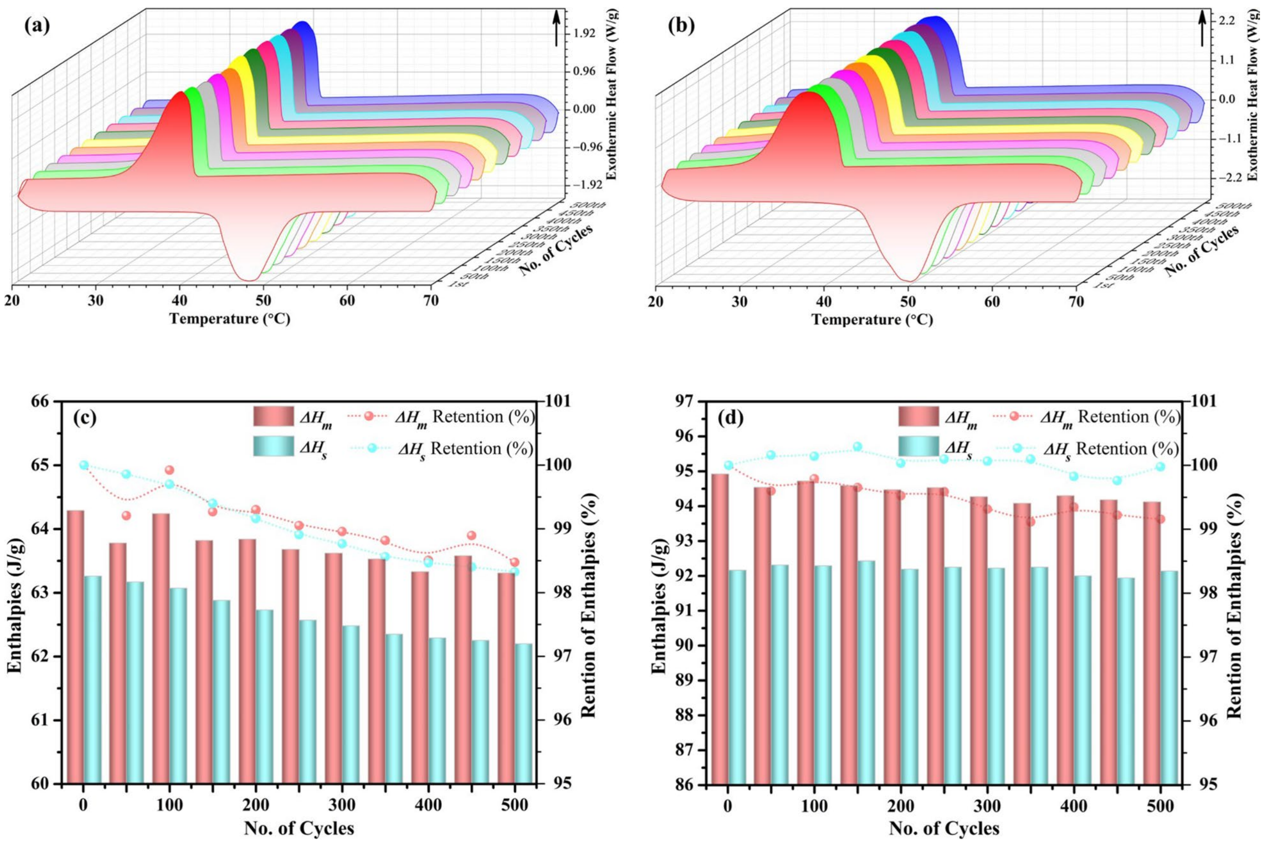

Fig. 11 Heat charging-discharging congruencies over 500 thermal cycles for (**a**) NBL3-2 and (**b**) NBL5-2, along with the corresponding enthalpy retention and enthalpy retention percentages for (**c**) NBL3-2 and (**d**) NBL5-2

to 94.12 J/g and solidification enthalpy declining from 92.16 J/g to 92.14 J/g. The enthalpy retention percentages after 500 cycles were computed as 98.48% for melting and 98.32% for solidification in NBL3-2, while for NBL5-2, they were 99.16% and 99.98%, respectively. These retention values fall within experimental error limits, rendering the enthalpy reductions negligible and accentuating the exceptional durability of the composites under prolonged cyclic exposure.

The extraordinary thermal cycle endurance of the NBL3-2 and NBL5-2 composite PCMs is primarily attributed to the previously discussed physical interactions (Sect. 3.6), including surface tension effects, capillary forces, spatial confinement within biochar pores, van der Waals interactions, and strong interfacial bonding between the PCM molecules and biochar functional groups (Mandal et al. 2023b; Mandal et al. 2022a, b). The pronounced thermal stability of these composites positions them as highly viable candidates for a spectrum of TES applications, spanning across building materials (Jin et al. 2021; Xie et al. 2020b), absorption cooling technologies (Agyenim 2016; Hirmiz et al. 2018), waste heat recovery systems (Mahmoud et al. 2021; Omara 2021), and solar-based heating systems (Ali 2022; Waqas and Kumar 2013). This exceptional phase change stability over extended thermal cycles not only ensures energy efficiency but also enhances the long-term viability of these materials in sustainable energy applications.

3.9 Leakage resilience performance

The shape-stabilized composites, along with pure LA, were further evaluated for their leakage resistance at different temperatures, and the corresponding images from the test are presented in Fig. 12. To assess the leakage resilience, 1 g of each sample was placed separately on Whatman filter paper and subjected to a controlled heating test on an electrical heating plate. The test was conducted at room temperature (25 ℃) and at an elevated temperature of 55 ℃, which is significantly higher than the T_m of LA (47.57 ℃). The leakage behavior was visually inspected based on the presence or absence of oil stains on the filter paper. As observed in Fig. 12, no visible stains or leakage were present at 25 ℃, indicating that all samples remained solid and stable at ambient conditions. However, as the temperature reached the T_m of pure LA, it began to liquefy, visibly staining the filter paper,

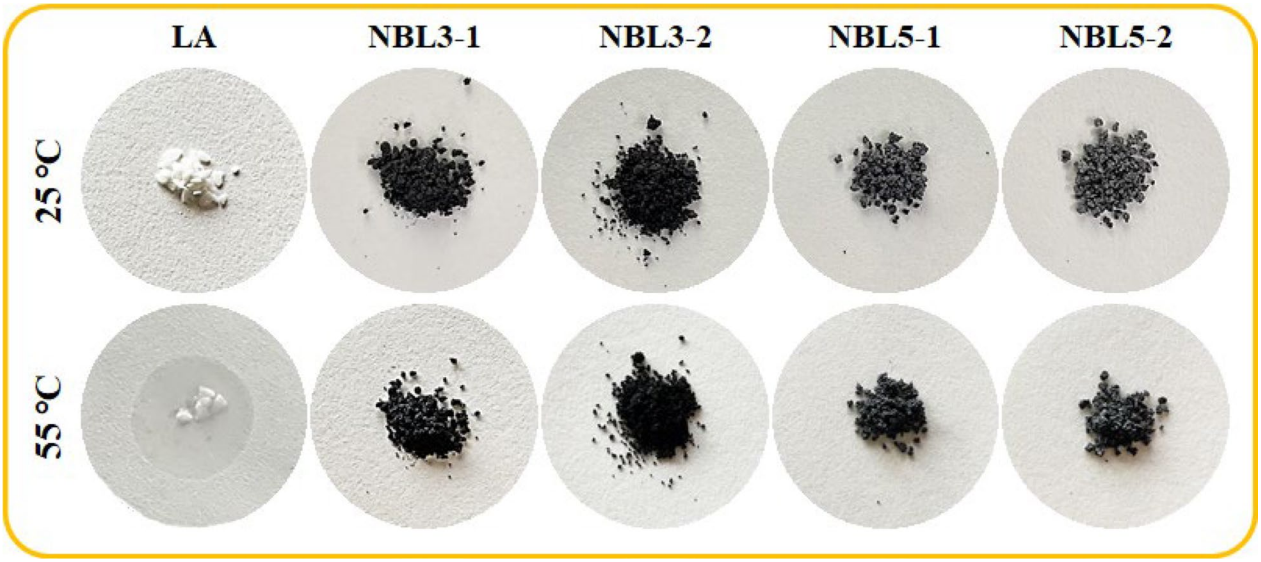

Fig. 12 Leakage resilience tests of LA and biochar composite PCMs at 25 and 55 ℃

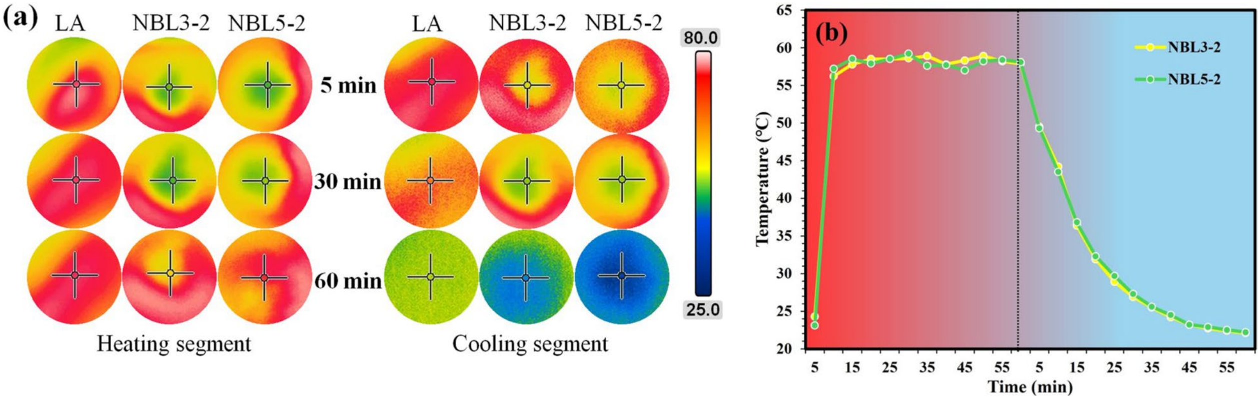

Fig. 13 **a** IR thermal imaging and temperature–time profile of LA, NBL3-2, and NBL5-2, **b** heat absorption, retention, and controlled dissipation during heating and cooling cycles

confirming its inability to maintain structural integrity in its pure form. In contrast, the shape-stabilized LA composites with NB-300 and NB-500 biochars exhibited exceptional thermal stability and retained their structural integrity even at 55 °C, with no signs of leakage. This clearly demonstrates the effectiveness of both biochars in form-stabilizing LA, preventing phase separation, and ensuring shape retention even beyond its melting point. Consequently, these results validate that NB-300 and NB-500 serve as highly efficient supporting matrices for LA, making them promising candidates for TES applications where leakage prevention and structural stability are crucial.

The dynamic thermal performance of the synthesized composite materials was assessed using an infrared camera, with each sample weighing 1 g (Fig. 13a). During the heating phase, the thermal images revealed that pure LA rapidly absorbed heat, reaching thermal equilibrium faster than the biochar-stabilized composites. This rapid temperature rise indicated LA's low thermal resistance and fast phase transition. In contrast, NBL3-2 and NBL5-2 exhibited a more gradual temperature increase, demonstrating enhanced thermal stability due to the biochar matrix, which acted as a thermal buffer, slowing heat transfer and promoting uniform heat distribution. This thermal regulation effect minimizes temperature gradients within the material. The temperature–time profile (Fig. 13b) further supported these findings, showing that NBL3-2 and NBL5-2 stabilize just above 55 ℃, highlighting their effective thermal absorption.

During the cooling phase, pure LA gradually lost heat and returned to a lower temperature over an extended period, reflecting its limited heat transfer efficiency. In contrast, the biochar-stabilized composites exhibited steady heat retention and a controlled temperature decline, demonstrating superior thermal energy storage and release capabilities. The temperature–time graph confirmed that NBL3-2 and NBL5-2 facilitated gradual heat dissipation, indicating that biochar effectively captured and slowly released thermal energy. This controlled thermal response makes these composites highly suitable for thermal management applications, offering improved phase change stability and energy efficiency.

4 Conclusions

In pursuit of carbon neutrality, this study developed biochar-based phase change material (PCM) composites by synthesizing biochar from Neem seed waste at two different pyrolysis temperatures and impregnating it with LA. Structural, chemical, and thermal analyses confirmed their effectiveness for thermal energy storage. The primary findings of this study are as follows:

(i) The textural characteristics of the biochars by BET analysis revealed that both the biochars possess porous structures. The adsorption–desorption isotherms of the biochar synthesized at a higher pyrolysis temperature exhibit a significantly larger surface area (668 m^2/g) and correspond to Type IV behavior with H3 hysteresis, characteristic of micromesoporous structures, which ensures effective accommodability of LA within the biochar matrix.

(ii) Microscopic examination confirmed a well-connected porous structure, and that biochar endures morphological transformations with increasing pyrolysis temperature, leading to a more developed porous network.

(iii) FTIR and EDS analyses confirmed that NB-500 biochar, pyrolyzed at a higher temperature, contains more nitrogen-containing functional groups, enhancing its surface functionality and interaction with PCMs.

(iv) Spectroscopic analysis identified alkyl, carboxyl, and hydroxyl groups in LA and biochar-PCM composites. The emergence of amide-like peaks in NB-500-based composites suggests nitrogen-mediated interactions, contributing to PCM stabilization.

(v) Thermal characterization indicated high latent heat storage, efficient PCM impregnation, and thermal stability. The highest R_s value (50.92) for NBL5-2 aligns with previous biochar-based PCMs. DSC confirms phase transition consistency, while TGA revealed delayed decomposition, ensuring long-term reliability for applications.

(vi) Leakage tests confirmed that the biochar effectively stabilizes LA, preventing seepage even at elevated temperatures. The composites retain structural integrity under thermal cycling conditions, demonstrating their durability in long-term applications.

(vii) Infrared thermal imaging and temperature–time analysis demonstrated controlled heat absorption and release, minimizing thermal fluctuations. The PCM composites exhibit superior thermal regulation over pure LA, ensuring gradual energy release for efficient thermal management.

(viii) The synthesized biochar-PCM composites provide a sustainable, cost-effective approach for thermal energy storage, offering significant potential in energy-efficient buildings, passive cooling systems, electronic thermal management, and renewable energy integration. Their eco-friendly nature aligns with global carbon neutrality goals, promoting sustainable energy solutions.

Acknowledgements
This work was partly supported by the Institute of Information & Communications Technology Planning & Evaluation (IITP) grant funded by the Korea government (MSIT) (No. RS-2022- 00155885, Artificial Intelligence Convergence Innovation Human Resources Development (Hanyang University ERICA)) and Hanyang University (HY-2024-0560).

Author contributions
Soumen Mandal: Conceptualization, Data curation, Formal analysis, Methodology, Investigation, Writing—original draft, Writing—review & editing. Avinash C. Mendhe: Formal analysis, Writing—review & editing. Taejoon Park: Project administration, Funding acquisition, Review & editing. Han-Seung Lee: Project administration, Funding acquisition, Review & editing. All authors read and approved the final manuscript.

Funding
Not applicable.

Data availability
The datasets used or analyzed during the current study are available from the corresponding author upon reasonable request.

Declarations

Competing interests
The authors declare that they have no known competing financial interests or personal relationships that could have appeared to influence the work reported in this paper.

Author details
[1]Industry-University Cooperation Foundation, Hanyang University ERICA, 1271 Sa-3-Dong, Sangnok-Gu, Ansan 15588, South Korea. [2]Department of Electronic Engineering, Institute for Wearable Convergence Electronics, Kyung Hee University, 1732 Deogyeong-daero, Giheung-Gu, Yongin 17104, Republic of Korea. [3]Department of Robotics Engineering, Hanyang University, 55 Hanyangdaehak-Ro, Ansan, Gyeonggi-Do 15588, South Korea. [4]Department of Architectural Engineering, Hanyang University, 1271 Sa 3-Dong, Sangnok-Gu, Ansan-Si 15588, South Korea.

Received: 1 March 2025 Revised: 5 September 2025 Accepted: 8 September 2025

References

Abdeen SA, Hefni HH, Awadallah-F A, El-Rahman NRA (2023) The synergistic effect of biochar and poly (2-ethyl-2-oxazoline)/poly (2-hydroxyethylmethacarylate)/chitosan) hydrogels on saline soil properties and carrot productivity. Chem Biol Technol Agric 10(1):68

Abdu YA, Hawthorne FC, Varela ME (2018) Infrared spectroscopy of carbonaceous-chondrite inclusions in the Kapoeta meteorite: discovery of nanodiamonds with new spectral features and astrophysical implications. Astrophys J Lett 856(1):L9

Agyenim F (2016) The use of enhanced heat transfer phase change materials (PCM) to improve the coefficient of performance (COP) of solar powered LiBr/H2O absorption cooling systems. Renew Energy 87:229–239

Ali HM (2022) Phase change materials based thermal energy storage for solar energy systems. J Build Eng 56:104731

Ambroz F, Macdonald TJ, Martis V, Parkin IP (2018) Evaluation of the BET theory for the characterization of Meso and microporous MOFs. Small Method 2(11):1800173

Ariyanta HA, Ivandini TA, Yulizar Y (2021) Novel NiO nanoparticles via phytosynthesis method: structural, morphological and optical properties. J Mol Struct 1227:129543

Armynah B, Tahir D, Tandilayuk M, Djafar Z, Piarah WH (2019) Potentials of biochars derived from bamboo leaf biomass as energy sources: effect of temperature and time of heating. Int J Biomater 2019(1):3526145

Atinafu DG, Chang SJ, Kim K-H, Kim S (2020) Tuning surface functionality of standard biochars and the resulting uplift capacity of loading/energy storage for organic phase change materials. Chem Eng J 394:125049

Atinafu DG, Yun BY, Kim YU, Wi S, Kim S (2021) Introduction of eicosane into biochar derived from softwood and wheat straw: influence of porous structure and surface chemistry. Chem Eng J 415:128887

Atinafu DG, Choi JY, Nam J, Kang Y, Kim S (2025) Insights into the effects of biomass feedstock and pyrolysis conditions on the energy storage capacity and durability of standard biochar-based phase-change composites. Biochar 7(1):18

Bachs-Herrera A, Vidal-Daza I, Boz EB, Forner-Cuenca A, Martin-Martinez FJ (2024) Understanding the role of nitrogen-doping and surface topology in the binding of Fe (iii)/Fe (ii) to biobased carbon electrodes. Energ Adv 3(6):1271–1282

Bläker C, Muthmann J, Pasel C, Bathen D (2019) Characterization of activated carbon adsorbents–state of the art and novel approaches. ChemBioEng Rev 6(4):119–138

Celso Goncalves A, Zimmermann J, Schwantes D, Tarley CRT, Conradi Junior E, Dias H, de Oliveira V, Campagnolo MA, Ziemer GL (2022) Renewable eco-friendly activated biochar from tobacco: kinetic, equilibrium and thermodynamics studies for chlorpyrifos removal. Sep Sci Technol 57(2):159–179

Chen Y, Cui Z, Ding H, Wan Y, Tang Z, Gao J (2018) Cost-effective biochar produced from agricultural residues and its application for preparation of high performance form-stable phase change material via simple method. Int J Mol Sci 19(10):3055

Chen L, Msigwa G, Yang M, Osman AI, Fawzy S, Rooney DW, Yap P-S (2022) Strategies to achieve a carbon neutral society: a review. Environ Chem Lett 20(4):2277–2310

Chien F, Hsu C-C, Ozturk I, Sharif A, Sadiq M (2022) The role of renewable energy and urbanization towards greenhouse gas emission in top Asian countries: evidence from advance panel estimations. Renew Energy 186:207–216

Choi Y-K, Srinivasan R, Kan E (2020) Facile and economical functionalized hay biochar with dairy effluent for adsorption of tetracycline. ACS Omega 5(27):16521–16529

Cole EJ, Zandvakili OR, Xing B, Hashemi M, Herbert S, Mashayekhi HH (2019) Dataset on the effect of hardwood biochar on soil gravimetric moisture content and nitrate dynamics at different soil depths with FTIR analysis of fresh and aged biochar. Data Brief 25:104073

Dehkhoda AM, Ellis N, Gyenge E (2014) Electrosorption on activated biochar: effect of thermo-chemical activation treatment on the electric double layer capacitance. J Appl Electrochem 44:141–157

Ehsani A, Parsimehr H (2020) Electrochemical energy storage electrodes from fruit biochar. Adv Colloid Interface Sci 284:102263

Elnour AY, Alghyamah AA, Shaikh HM, Poulose AM, Al-Zahrani SM, Anis A, Al-Wabel MI (2019) Effect of pyrolysis temperature on biochar microstructural evolution, physicochemical characteristics, and its influence on biochar/polypropylene composites. Appl Sci 9(6):1149

Farghali M, Osman AI, Chen Z, Abdelhaleem A, Ihara I, Mohamed IM, Yap P-S, Rooney DW (2023) Social, environmental, and economic consequences of integrating renewable energies in the electricity sector: a review. Environ Chem Lett 21(3):1381–1418

Fu B, Ge C, Yue L, Luo J, Feng D, Deng H, Yu H (2016) Characterization of biochar derived from pineapple peel waste and its application for sorption of oxytetracycline from aqueous solution. Bioresour 11(4):9017–9035

Gipson K, Stevens K, Brown P (2015) Ballato J (2015) Infrared spectroscopic characterization of photoluminescent polymer nanocomposites. J Spectrosc 1:489162

Grzelec M (2024) Application of attenuated total reflectance—Fourier transform infrared spectroscopy—(ATR-FTIR) and principal component analysis (PCA) in identification of copying pencils on different paper substrates. Herit Sci 12(1):269

Gu X, Liu P, Liu C, Peng L, He H (2019) A novel form-stable phase change material of palmitic acid-carbonized pepper straw for thermal energy storage. Mater Lett 248:12–15

Gurav R, Bhatia SK, Choi T-R, Kim HJ, Choi Y-K, Lee H-J, Ham S, Cho JY, Kim SH, Lee SH (2022) Adsorptive removal of synthetic plastic components bisphenol-A and solvent black-3 dye from single and binary solutions using pristine pinecone biochar. Chemosphere 296:134034

Gutsch M, Leker J (2024) Costs, carbon footprint, and environmental impacts of lithium-ion batteries–from cathode active material synthesis to cell manufacturing and recycling. Appl Energy 353:122132

Hanafi NAM, Abdulhameed AS, Jawad AH, ALothman ZA, Yousef TA, Al Duaij O, Alsaiari NS (2024) Optimized removal process and tailored adsorption mechanism of crystal violet and methylene blue dyes by activated carbon derived from mixed orange peel and watermelon rind using microwave-induced ZnCl2 activation. Biomass Convers Biorefin 14(22):28415–28427

Hao Y, Li X, Murshed M (2023) Role of environmental regulation and renewable energy technology innovation in carbon neutrality: a sustainable investigation from China. Energy Strategy Rev 48:101114

Hekimoğlu G, Sarı A, Kar T, Keleş S, Kaygusuz K, Yıldırım N, Tyagi VV, Sharma RK, Saleh TA (2021) Carbonized waste hazelnut wood-based shape-stable composite phase change materials for thermal management implementations. Int J Energy Res 45(7):10271–10284

Hirmiz R, Lightstone M, Cotton J (2018) Performance enhancement of solar absorption cooling systems using thermal energy storage with phase change materials. Appl Energy 223:11–29

Ishak S, Mandal S, Lee H-S, Singh JK (2020) Microencapsulation of stearic acid with SiO2 shell as phase change material for potential energy storage. Sci Rep 10(1):15023

Ishak S, Mandal S, Lee H-S, Singh JK (2021a) pH-controlled synthesis of sustainable lauric acid/SiO2 phase change material for scalable thermal energy storage. Sci Rep 11(1):15012

Ishak S, Mandal S, Lee H-S, Singh JK (2021b) Effect of core-shell ratio on the thermal energy storage capacity of SiO2 encapsulated lauric acid. J Energy Storage 42:103029

Ishak S, Lgaz H, Mandal S, Adnin RJ, Lee D-E, Lee H-S, Harmay NSM, Abdullah MMAB, Wang X-Y, Yang H-M (2023) Multi-technique investigation on the surface interaction of diatomaceous earth with organic phase change material: experimental and molecular dynamics aspects. J Mol Liq 391:123292

Ishak S, Mandal S, Lgaz H, Atinafu DG, Mohammad Harmay NS, Lee H-S, Abdul Shukor Lim N, Abdullah MMAB, Yang H-M (2024) Microscopic molecular insights of different carbon chain fatty acids on shape-stabilized phase change composite. J Therm Anal Calorim 149(17):9203–9221

Islam MA, Ali MN, Al Mamun A, Hossain MS, Maruf MH, Shihavuddin A (2024) Optimizing energy solutions: a techno-economic analysis of solar-wind hybrid power generation in the coastal regions of Bangladesh. Energ Convers Manag X 22:100605

Ismail M, Dincer I, Bicer Y, Saghir M (2024) Assessment of a solar-powered trigeneration plant integrated with thermal energy storage using phase change materials. Process Saf Environ Prot 191:1339–1352

Jafarian M, Assareh E, Ershadi A, Wang X (2024) Optimal integration of efficient energy storage and renewable sources in hybrid energy systems: a novel optimization and dynamic evaluation strategy. J Energy Storage 101:113880

Janu R, Mrlik V, Ribitsch D, Hofman J, Sedláček P, Bielská L, Soja G (2021) Biochar surface functional groups as affected by biomass feedstock, biochar composition and pyrolysis temperature. Carbon Res Convers 4:36–46

Jeon J, Park JH, Wi S, Yang S, Ok YS, Kim S (2019) Latent heat storage biocomposites of phase change material-biochar as feasible eco-friendly building materials. Environ Res 172:637–648

Jia Y, Jiang Y, Pan Y, Zou X, Zhang Q, Gao X, Zhang J, Yu K, Yang Y, Liu Y (2024) Recent advances in energy storage and applications of form-stable phase change materials with recyclable skeleton. Carbon Neutraliz 3(2):313–343

Jiang W, Zhu T, Chen J, Liu Q, Liu Y, Huang Z, Qi X, Wang Y (2024) Phase change foam with temperature-adaptive radiative cooling feature for all-day building energy saving. Chem Eng J 502:157862

Jin W, Jiang L, Chen L, Yin T, Gu Y, Guo M, Yan X, Ben X (2021) Enhancement of thermal conductivity by graphene as additive in lauric-stearic acid/treated diatomite composite phase change materials for heat storage in building envelope. Energy Build 246:111087

Katish M, Allen S, Squires A, Ferrandiz-Mas V (2024) Experimental study of phase change material (PCM) biochar composite for net-zero built environment applications. Clean Mater 14:100274

Koh SL, Jia F, Gong Y, Zheng X, Dolgui A (2023) Achieving carbon neutrality via supply chain management: position paper and editorial for IJPR special issue. Taylor & Francis, Abingdon-on-Thames, pp 6081–6092

Kouchachvili L, Gagnon-Caya G, Djebbar R (2024) Wood-derived biochar as a matrix for cost-effective and high-performing composite thermal energy storage materials. J Porous Mater. https://doi.org/10.1007/s10934-024-01638-0

Kumar A, Kumar R (2024) Enhancement and estimation of thermo-physical properties of organic-phase change materials (O-PCMs) and their applications in solar thermal technologies: a review. J Energy Storage 101:113741

Liang Q, Pan D, Zhang X (2023) Construction and application of biochar-based composite phase change materials. Chem Eng J 453:139441

Lima DR, Hosseini-Bandegharaei A, Thue PS, Lima EC, de Albuquerque YR, dos Reis GS, Umpierres CS, Dias SL, Tran HN (2019) Efficient acetaminophen removal from water and hospital effluents treatment by activated carbons derived from Brazil nutshells. Coll Surf A Physicochem Engin Asp 583:123966

Lin Z, Li D, Zou Y (2023) Energy efficiency of lithium-ion batteries: influential factors and long-term degradation. J Energy Storage 74:109386

Liu S, Peng S, Zhang B, Xue B, Yang Z, Wang S, Xu G (2022) Effects of biochar pyrolysis temperature on thermal properties of polyethylene glycol/biochar composites as shape-stable biocomposite phase change materials. RSC Adv 12(16):9587–9598

Ma Y, Shen J, Li T, Sheng X, Chen Y (2024) A "net-ball" structure fiber membrane with electro-/photo-thermal heating and phase change synchronous temperature regulation capacity via electrospinning. Sol Energ Mater Sol Cell 276:113078

Mahmoud M, Ramadan M, Pullen K, Abdelkareem MA, Wilberforce T, Olabi AG, Naher S (2021) Waste heat recovery applications incorporating phase change materials. Encyclopedia of smart materials. Elsevier, Amsterdam, pp 513–521

Mandal S (2024) Advancements in phase change materials: stabilization techniques and applications. Prabha Mater Sci Lett 3:254–268

Mandal S, Ishak S, Lee D-E, Park T (2022a) Optimization of eco-friendly *Pinus resinosa* biochar-dodecanoic acid phase change composite for the cleaner environment. J Energy Storage 55:105414

Mandal S, Ishak S, Lee D-E, Park T (2022b) Shape-stabilized orange peel/myristic acid phase change materials for efficient thermal energy storage application. Energy Rep 8:9618–9628

Mandal S, Ishak S, Singh JK, Lee D-E, Park T (2022c) Synthesis and application of paraffin/silica phase change nanocapsules: experimental and numerical approach. J Energy Storage 51:104407

Mandal S, Ishak S, Adnin RJ, Lee D-E, Park T (2023a) An approach to utilize date seeds biochar as waste material for thermal energy storage applications. J Energy Storage 68:107739

Mandal S, Ishak S, Ariffin MAM, Lee D-E, Park T (2023b) Effect of pore structure on the thermal stability of shape-stabilized phase change materials. J Mater Res Technol 25:465–479

Martínez FR, Borri E, Ushak S, Kala SM, Prieto C, Cabeza LF (2025) Experimental characterization of phase change materials for thermal energy storage in the temperature range between 270° C and 400° C. Energy 314:134243

Melo LC, Coscione AR, Abreu CA, Puga AP, Camargo OA (2013) Influence of pyrolysis temperature on cadmium and zinc sorption capacity of sugar cane straw-derived biochar. BioResour. https://doi.org/10.15376/biores.8.4.4992-5004

Mendoza R, Oliva J, Rodriguez-Gonzalez V (2022) Effect of the micro-, meso- and macropores on the electrochemical performance of supercapacitors: a review. Int J Energy Res 46(6):6989–7020

Minaei S, Benis KZ, McPhedran KN, Soltan J (2023) Evaluation of a ZnCl2-modified biochar derived from activated sludge biomass for adsorption of sulfamethoxazole. Chem Eng Res des 190:407–420

Moodley C, Mallick K, Muller A, Williams DBG (2025) Transition-and lanthanide-metal-based coordination polymers offer efficient methylene blue adsorption. ChemSelect 10(4):e202402762

Muhammad N, Ge L, Chan WP, Khan A, Nafees M, Lisak G (2022) Impacts of pyrolysis temperatures on physicochemical and structural properties of green waste derived biochars for adsorption of potentially toxic elements. J Environ Manage 317:115385

Nirbheram JS, Mahesh A, Bhimaraju A (2024) Techno-economic optimization of standalone photovoltaic-wind turbine-battery energy storage system hybrid energy system considering the degradation of the components. Renew Energy 222:119918

Nkomo N, Odindo AO, Musazura W, Missengue R (2021) Optimising pyrolysis conditions for high-quality biochar production using black soldier fly larvae faecal-derived residue as feedstock. Heliyon. https://doi.org/10.1016/j.heliyon.2021.e07025

Omara AA (2021) Phase change materials for waste heat recovery in internal combustion engines: a review. J Energy Storage 44:103421

Ovchinnikov OV, Evtukhova AV, Kondratenko TS, Smirnov MS, Khokhlov VY, Erina OV (2016) Manifestation of intermolecular interactions in FTIR spectra of methylene blue molecules. Vibr Spectrosc 86:181–189

Parsimehr H, Ehsani A (2020a) Corn-based electrochemical energy storage devices. Chem Record 20(10):1163–1180

Parsimehr H, Ehsani A (2020b) Algae-based electrochemical energy storage devices. Green Chem 22(23):8062–8096

Parsimehr H, Ehsani A, Goharshenas Moghadam S, Arachchige Dumith Madushanka Jayathilaka W, Ramakrishna S (2021) Energy harvesting/storage and environmental remediation via hot drinks wastes. Chem Record 21(5):1098–1118

Patel D, Wei W, Singh H, Xu K, Beck C, Wildy M, Schossig J, Hu X, Hyun DC, Chen W (2023) Efficient and secure encapsulation of a natural phase change material in nanofibers using coaxial electrospinning for sustainable thermal energy storage. ACS Sustain Chem Eng 11(31):11570–11579

Petrovic B, Gorbounov M, Soltani SM (2022) Impact of surface functional groups and their introduction methods on the mechanisms of CO2 adsorption on porous carbonaceous adsorbents. Carbon Capture Sci Technol 3:100045

Pezoti O Jr., Cazetta AL, Souza IP, Bedin KC, Martins AC, Silva TL, Almeida VC (2014) Adsorption studies of methylene blue onto ZnCl2-activated carbon produced from buriti shells (*Mauritia flexuosa* L.). J Ind Eng Chem 20(6):4401–4407

Pietrzak R (2009) XPS study and physico-chemical properties of nitrogen-enriched microporous activated carbon from high volatile bituminous coal. Fuel 88(10):1871–1877

Pimentel CH, Díaz-Fernández L, Gómez-Díaz D, Freire MS, González-Álvarez J (2023a) Separation of CO2 using biochar and KOH and ZnCl2 activated carbons derived from pine sawdust. J Environ Chem Eng 11(6):111378

Pimentel CH, Freire MS, Gómez-Díaz D, González-Álvarez J (2023b) Preparation of activated carbon from pine (*Pinus radiata*) sawdust by chemical activation with zinc chloride for wood dye adsorption. Biomass Convers Biorefin 13(18):16537–16555

Rambhatla N, Panicker TF, Mishra RK, Manjeshwar SK, Sharma A (2025) Biomass pyrolysis for biochar production: study of kinetics parameters and effect of temperature on biochar yield and its physicochemical properties. Results Eng 25:103679

Saied ME, Shaban SA, Mostafa MS, Naga AOAE (2024) Efficient adsorption of acetaminophen from the aqueous phase using low-cost and renewable adsorbent derived from orange peels. Biomass Convers Biorefin 14(2):2155–2172

Sánchez-Machado DI, López-Cervantes J, Escárcega-Galaz AA, Campas-Baypoli ON, Martínez-Ibarra DM, Rascón-León S (2024) Measurement of the degree of deacetylation in chitosan films by FTIR, ^{1}H NMR and UV spectrophotometry. MethodsX 12:102583

Sangeetha Piriya R, Jayabalakrishnan RM, Maheswari M, Boomiraj K, Oumabady S (2021) Coconut shell derived ZnCl2 activated carbon for malachite green dye removal. Water Sci Technol 83(5):1167–1182

Sayğılı H, Güzel F (2016) High surface area mesoporous activated carbon from tomato processing solid waste by zinc chloride activation: process optimization, characterization and dyes adsorption. J Clean Prod 113:995–1004

Sayğılı H, Güzel F, Önal Y (2015) Conversion of grape industrial processing waste to activated carbon sorbent and its performance in cationic and anionic dyes adsorption. J Clean Prod 93:84–93

Senadheera SS, Withana PA, Lim JY, You S, Chang SX, Wang F, Rhee JH, Ok YS (2024) Carbon negative biochar systems contribute to sustainable urban green infrastructure: a critical review. Green Chem. https://doi.org/10.1039/D4GC03071K

Serat Z (2024) Optimizing renewable energy systems for 100% clean energy target: a comparative study of solar, hydro, pumped hydro, and battery storage technologies. J Energy Storage 104:114441

Shankar P, Rayappan JBB (2017) Room temperature ethanol sensing properties of ZnO nanorods prepared using an electrospinning technique. J Mater Chem C 5(41):10869–10880

Sharifah I, Nurul AT, Khairusshima MN (2017) Thermal modelling and analysis of batik canting design. Procedia Eng 184:326–333

Sharma R, Khalid M, Ismail MY (2024) Enhancing surface properties of circular carbon biochar derived from spent coffee beans through ZnCl2/KOH activation. Bioenergy Res 18(1):2

Shukla U (2024) Fourier transform infrared spectroscopy: a power full method for creating fingerprint of molecules of nanomaterials. J Mol Struct. https://doi.org/10.1016/j.molstruc.2024.140454

Siipola V, Tamminen T, Källi A, Lahti R, Romar H, Rasa K, Keskinen R, Hyväluoma J, Hannula M, Wikberg H (2018) Effects of biomass type, carbonization process, and activation method on the properties of bio-based activated carbons. BioResour. https://doi.org/10.15376/biores.13.3.5976-6002. (**North Carolina State University: Raleigh**)

Soni K, Panwar NL (2024) Revolutionizing Thermal Energy Storage: An Overview of Porous Support Materials for Advanced Composite Phase Change Materials (PCMs). Progress in Engineering Science. https://doi.org/10.1016/j.pes.2024.100023

Suhaimi A, Abdulhameed AS, Jawad AH, Yousef TA, Al Duaij O, ALOthman ZA, Wilson LD (2022) Production of large surface area activated carbon from a mixture of carrot juice pulp and pomegranate peel using microwave radiation-assisted ZnCl2 activation: an optimized removal process and tailored adsorption mechanism of crystal violet dye. Diamond Relat Mater 130:109456

Tan B, Huang Z, Yin Z, Min X, Liu Yg, Wu X, Fang M (2016) Preparation and thermal properties of shape-stabilized composite phase change materials based on polyethylene glycol and porous carbon prepared from potato. RSC Adv 6(19):15821–15830

Thongsamer T, Vinitnantharat S, Pinisakul A, Werner D (2022) Chitosan impregnation of coconut husk biochar pellets improves their nutrient removal from eutrophic surface water. Sustain Environ Res 32(1):39

Tyagi V, Chopra K, Kalidasan B, Chauhan A, Stritih U, Anand S, Pandey A, Sarı A, Kothari R (2021) Phase change material based advance solar thermal energy storage systems for building heating and cooling applications: a prospective research approach. Sustain Energy Technol Assess 47:101318

Varela CF, Moreno-Aldana L, Agámez-Pertuz YY (2024) Adsorption of pharmaceutical pollutants on ZnCl2-activated biochar from corn cob: efficiency, selectivity and mechanism. J Bioresour Bioprod 9(1):58–73

Wan Y-c, Chen Y, Cui Z-x, Ding H, Gao S-f, Han Z, Gao J-k (2019) A promising form-stable phase change material prepared using cost effective pinecone biochar as the matrix of palmitic acid for thermal energy storage. Sci Rep 9(1):11535

Wang T, Liu J, Zhang Y, Zhang H, Chen W-Y, Norris P, Pan W-P (2018) Use of a non-thermal plasma technique to increase the number of chlorine active sites on biochar for improved mercury removal. Chem Eng J 331:536–544

Wang Z, Sun S, Lin X, Liu C, Tong N, Sui Q, Li Z (2019) A remote integrated energy system based on cogeneration of a concentrating solar power plant and buildings with phase change materials. Energy Convers Manage 187:472–485

Wang F, Harindintwali JD, Yuan Z, Wang M, Wang F, Li S, Yin Z, Huang L, Fu Y, Li L (2021) Technologies and perspectives for achieving carbon neutrality. Innov (Camb). https://doi.org/10.1016/j.xinn.2021.100180

Wang C, Jiang H, Miao E, Wang Y, Zhang T, Xiao Y, Liu Z, Ma J, Xiong Z, Zhao Y (2024) Accelerated CO2 mineralization technology using fly ash as raw material: recent research advances. Chem Eng J. https://doi.org/10.1016/j.cej.2024.150676

Waqas A, Kumar S (2013) Phase change material (PCM)-based solar air heating system for residential space heating in winter. Int J Green Energy 10(4):402–426

Xia D, Tan F, Zhang C, Jiang X, Chen Z, Li H, Zheng Y, Li Q, Wang Y (2016) ZnCl2-activated biochar from biogas residue facilitates aqueous As (III) removal. Appl Surf Sci 377:361–369

Xie B, Li C, Zhang B, Yang L, Xiao G, Chen J (2020a) Evaluation of stearic acid/coconut shell charcoal composite phase change thermal energy storage materials for tankless solar water heater. Energy Built Environ 1(2):187–198

Xie N, Niu J, Zhong Y, Gao X, Zhang Z, Fang Y (2020b) Development of polyurethane acrylate coated salt hydrate/diatomite form-stable phase change material with enhanced thermal stability for building energy storage. Constr Build Mater 259:119714

Xing Q, Zhang L, Redman T, Qi S, Zhao F (2015) Nitric oxide regulates cell behavior on an interactive cell-derived extracellular matrix scaffold. J Biomed Mater Res A 103(12):3807–3814

Yan Q, Mu B (2025) Energy storage materials for phase change heat devices recovering industrial waste heat for heating purposes. Int Commun Heat Mass Transfer 160:108376

Yan L, Liu Y, Zhang Y, Liu S, Wang C, Chen W, Liu C, Chen Z, Zhang Y (2020) ZnCl2 modified biochar derived from aerobic granular sludge for developed microporosity and enhanced adsorption to tetracycline. Bioresour Technol 297:122381

Yan R, Huang Z, Chen Y, Zhang L, Sheng X (2024) Phase change composite based on lignin carbon aerogel/nickel foam dual-network for multisource energy harvesting and superb EMI shielding. Int J Biol Macromol 277:134233

Yang Y, Okonkwo EG, Huang G, Xu S, Sun W, He Y (2021) On the sustainability of lithium ion battery industry–a review and perspective. Energy Storage Mater 36:186–212

Yanghua C, Yuan L, Zhaohe W (2020) Preparation and characteristics of microencapsulated lauric acid as composite thermal energy storage materials. Mater Sci 26(1):88–93

Zakaria DS, Rozi SKM, Halim HNA, Mohamad S, Zheng GK (2024) New porous amine-functionalized biochar-based desiccated coconut waste as efficient CO2 adsorbents. Environ Sci Pollut Res 31(11):16309–16327

Zhang Y, Zhang J, Li X, Wu X (2019) Preparation of hydrophobic lauric acid/SiO2 shape-stabilized phase change materials for thermal energy storage. J Energy Storage 21:611–617

Zhang Y, Shen B, Ahmad MS, Zhou W, Khalid RR, Ibrahim M, Bokhari A (2023) A three-dimensional active biochar for sintering in steel industry and remove methylene blue by synergistic activation of H3PO4 and ZnCl2. Fuel 336:127079

Zhang Y, Yan J, Xie H, Luo J (2024a) Preparation and performance study of porous biochar-based shape-stabilized phase change materials for thermal energy storage. Biomass Convers Biorefin 15:1–17

Zhang Z, Zhao X, Zhang R, Cao J (2024b) Novel phase change materials with superior thermal conductivity and photothermal efficiency derived from preservative-treated wood biochar. Renew Energy 237:121724

Zou S, Sham ML, Xiao J, Leung LM, Lu J-X, Poon CS (2024a) Biochar-enabled carbon negative aggregate designed by core-shell structure: a novel biochar utilizing method in concrete. Constr Build Mater 449:138507

Zou X, Debiagi P, Amjed MA, Zhai M, Faravelli T (2024b) Impact of high-temperature biomass pyrolysis on biochar formation and composition. J Anal Appl Pyrolysis 179:106463